ENGINEERING

Multifunctional microrobot with real-time visualization and magnetic resonance imaging for chemoembolization therapy of liver cancer

Gwangjun Go[1,2,3], Ami Yoo[2], Kim Tien Nguyen[2], Minghui Nan[2], Bobby Aditya Darmawan[2,3], Shirong Zheng[2,3], Byungjeon Kang[2,4], Chang-Sei Kim[2,3], Doyeon Bang[2,4], Seonmin Lee[5], Kyu-Pyo Kim[5], Seong Soo Kang[6], Kyung Mi Shim[6], Se Eun Kim[6], Seungmin Bang[7], Deok-Ho Kim[1,8]*, Jong-Oh Park[2]*, Eunpyo Choi[2,3]*

Microrobots that can be precisely guided to target lesions have been studied for in vivo medical applications. However, existing microrobots have challenges in vivo such as biocompatibility, biodegradability, actuation module, and intra- and postoperative imaging. This study reports microrobots visualized with real-time x-ray and magnetic resonance imaging (MRI) that can be magnetically guided to tumor feeding vessels for transcatheter liver chemoembolization in vivo. The microrobots, composed of a hydrogel-enveloped porous structure and magnetic nanoparticles, enable targeted delivery of therapeutic and imaging agents via magnetic guidance from the actuation module under real-time x-ray imaging. In addition, the microrobots can be tracked using MRI as postoperative imaging and then slowly degrade over time. The in vivo validation of microrobot system–mediated chemoembolization was demonstrated in a rat liver with a tumor model. The proposed microrobot provides an advanced medical robotic platform that can overcome the limitations of existing microrobots and current liver chemoembolization.

INTRODUCTION

Microrobots have been developed for biomedical applications such as drug delivery, diagnostics, localized biopsy, and regenerative medicine (1). They can move freely and be guided wirelessly to the target area using several external actuation sources (e.g., chemical, acoustic, light, magnetic, microorganism, and combinational) with precise control (2–5). High controllability of microrobots enables their locomotion along complex and narrow tubes in the body during noninvasive surgery. Among microrobot applications, interventional procedures using microrobots are raising expectations as a next-generation medical treatment method because microrobots can be guided to the lesion site to perform diagnosis or drug delivery and perform a given task quickly and accurately (6, 7). Although most studies are in vitro studies, research groups are trying to verify the targeting and therapeutic effects of microrobots in vivo (fig. S1) (8–19).

The medical microrobot system required in vivo can be divided into fabrication, actuation, and imaging. Considering the fabrication of microrobots for implantation in the body, studies have tested microrobots with biocompatible and biodegradable materials (fig. S1). However, the biocompatibility and biodegradation of most microrobots have been evaluated by coculturing cells and microrobots in vitro (8–15). Only a few in vivo studies on microrobots have demonstrated their nontoxicity and degradation over time in each organ through inflammation tests and histological analysis (16–19). Therefore, before clinical trials with microrobots can be conducted, experiments verifying the nontoxicity and biodegradability of microrobots in vitro as well as in vivo are required. Furthermore, in the case of microrobot actuation, in vivo studies have reported that microrobots can move in organs such as the stomach (8), abdominal cavity (9), blood vessels (14, 15), brain (16), intestine (17, 19), and joint cavity (18) (fig. S1). However, most microrobot actuation modules have been designed without considering the surgical environment that includes patients, medical staff, and imaging equipment. Therefore, large-scale modifications from design to fabrication of the microrobot actuation module for large-animal experiments and clinical trials are unavoidable. To address this issue, a microrobot actuation module should be designed and fabricated considering clinical trials, including the microrobot operation environment and process from the preclinical test stage.

In terms of microrobot imaging, most studies have used postoperative imaging methods such as magnetic resonance imaging (MRI), x-ray computed tomography (CT), photoacoustic CT, and fluorescence imaging to verify the movement of microrobots in vivo (20, 21). However, the observation of microrobots using postoperative imaging methods with long scanning times cannot guarantee precise targeting in complex and narrow systems in the body (fig. S1) (8–11, 14, 15). Moreover, immediate action cannot be taken in emergencies such as microrobot targeting failure. Therefore, along with postoperative imaging, in vivo real-time imaging of microrobots is required for precise microrobot targeting and safety of interventional procedures. However, in vivo real-time imaging of microrobots remains a challenge, except for some organs that can be accessed by endoscopes because of the small size of microrobots and low detection resolution of imaging devices (18, 19).

In the case of the vascular system, optical visualization–based imaging devices cannot be used for microrobot tracking because of

[1]Department of Biomedical Engineering, Johns Hopkins University, Baltimore, MD 21205, USA. [2]Korea Institute of Medical Microbotics (KIMIRo), 43-26 Cheomdangwagi-ro, Buk-gu, Gwangju 61011, Korea. [3]School of Mechanical Engineering, Chonnam National University, 77 Yongbong-ro, Buk-gu, Gwangju 61186, Korea. [4]College of AI Convergence, Chonnam National University, Gwangju 34931, Korea. [5]Department of Oncology, Asan Medical Center, University of Ulsan College of Medicine, 88, Olympic-ro 43-gil, Songpa-Gu, Seoul 05505, Korea. [6]Department of Veterinary Surgery, College of Veterinary Medicine and Biomaterial R&BD Center, Chonnam National University, Gwangju 61186, Korea. [7]Division of Gastroenterology, Department of Internal Medicine, Yonsei University College of Medicine, Seoul 120-752, Korea. [8]Department of Medicine, Johns Hopkins School of Medicine, Baltimore, MD 21205, USA.
*Corresponding author. Email: dhkim@jhu.edu (D.-H.K.); jop@kimiro.re.kr (J.-O.P.); eunpyochoi@jnu.ac.kr (E.C.)

the complex structure of blood vessels and the inherent visible absorbance of blood. To overcome this limitation, several research groups have verified the movement of microrobots in blood vessels using imaging devices with high spatiotemporal resolution. For example, the real-time movements of nanorobots under magnetic guidance were observed ex vivo in a pig eyeball (22) and coronary artery (23) by ultrasound imaging. Moreover, the real-time movements of three-dimensional (3D) printed microrobots were monitored in vivo in a mouse portal vein (13) and ear vessel (12) by optical coherence tomography and photoacoustic imaging. Although optical coherent tomography and photoacoustic imaging have a high spatiotemporal resolution, they have a low penetration depth (maximum of 48 mm) (24), limiting real-time imaging of deep tissues in the body. For access to deeper vascular regions, a microrobot composed of biodegradable polymer and magnetic nanoparticles (MNPs) was developed for transcatheter arterial embolization (15, 25, 26). The researchers evaluated microrobot targeting through MRI as postoperative imaging, which showed that they were able to precisely transport robots in the targeted site in liver blood vessels of phantom, rabbit, and pig by using strong magnetic fields generated by an MRI scanner and a gradient coil. Although the robotic system showed high targeting efficiency of microrobots via postoperative imaging of microrobots in the target region of the liver, there were limits to demonstrate real-time imaging of microrobots and their biological and therapeutic results such as biocompatibility, biodegradation, and cancer-killing effects. Hence, the tracking of microrobots in blood vessels with real-time imaging is mostly ex vivo and has not been validated in deep organs, such as the liver and heart, which are accessible through blood vessels. Furthermore, because of these imaging limitations, no study has verified the targeting and therapeutic effects of microrobots injected into blood vessels in in vivo disease models.

Compared with particle-based anticancer drug delivery that circulates in the body's vasculature after intravenous administration, we focused on embolic beads being used in transcatheter arterial chemoembolization (TACE) for the treatment of liver cancer (27). In treating liver cancer, embolic beads carrying the anticancer drug are injected by a catheter guided around the tumor hepatic artery. The injected embolic beads occlude the tumor feeding vessel within a few seconds, and oxygen and nutrients delivered to the tumor are blocked. The injected drug not only stays around the tumor for a long time because of the blocked blood flow but also spreads less throughout the body compared to the drug administered intravenously. These vascular occlusion and drug release delay effects made embolic bead–based embolization a representative treatment method for liver cancer. Currently, during the TACE procedure, the catheter for embolic bead injection is adjusted to be positioned as close to the liver tumor as possible. However, the catheter cannot access vessels less than twice the diameter of the catheter (27, 28); only a 1.4-Fr microcatheter (outer diameter: 0.57 mm) can access the six branches (vessel diameter: 1.3 mm) of the human hepatic artery (29). On the basis of the clinically limited access of the catheter, embolic beads with a size range of 100 to 1000 μm are injected through the catheter and then pass through an additional two to four branches. However, a common TACE issue is that embolic beads may flow into nontarget blood vessels while passing through multiple branches (27, 30, 31). These nontargeted embolic beads cause embolism of untargeted sites within organs or other vital areas and consequently lead to unwanted damage to healthy tissues (27, 31). In terms of biodegradability of embolic agents including embolic beads, agents made from

biocompatible and biodegradable polymeric materials only temporarily occlude tumor blood vessels (from hours up to weeks), and then blood flow resumes in the vessels. These biodegradable embolic agents are being actively studied and used clinically (27, 30, 31). Furthermore, although not yet clinically approved, several efforts are being actively conducted to enable both real-time and postoperative imaging of biodegradable embolic agents. For example, several studies have shown that embolic agents loaded with radio-opaque or magnetic-responsive materials are capable of real-time x-ray imaging, MRI, and CT imaging, as well as vessel embolization and biodegradation (32–35).

Here, we present a multifunctional medical microrobot system capable of real-time and postoperative imaging for liver chemoembolization, including targeted vessel embolization and drug delivery, and an in vivo test to evaluate microrobot efficacy using a liver tumor model. Compared with medical microrobots developed to date, the proposed microrobot system enables real-time microrobot imaging in vivo and has an actuation module suitable for preclinical trials. Regarding liver tumor treatment, the microrobot system can provide additional functions to the clinically approved embolic microbeads used in TACE. The proposed microrobot system consists of a microrobot for targeting, intra- and postoperative imaging, and drug delivery and a magnetic actuation module for targeted delivery of the microrobot to the tumor feeding vessel (Fig. 1). The microrobot comprises a microbead and MNPs attached to the surface of the microbead [(1) of Fig. 1A]. Specifically, the microbead is composed of poly(lactic-co-glycolic acid) (PLGA) microspheres with porous microstructure and gelatin beads. The porous microstructure of PLGA enhances the structural stability of the microbead, and gelatin beads help attach MNPs and load therapeutic and imaging agents. Here, PLGA and gelatin are representative synthetic and natural polymers with biocompatibility and biodegradability, respectively. MNPs adsorbed on the microbead enable MRI postoperatively and microrobot locomotion by external magnetic fields. The MNPs are prepared by sequentially modifying polydopamine (PDA), polyethylene glycol (PEG), and folic acid (FA) on the surface of Fe_3O_4 nanoparticles. The microrobot has sufficient magnetic properties for magnetic actuation and MRI, as well as biocompatibility and biodegradability. In addition to driving the microrobot, therapeutic and imaging agents are loaded into the microrobot to enable tumor treatment and real-time imaging [(2) of Fig. 1A]. In this study, doxorubicin (DOX) and fluorouracil (5-FU), which are representative anticancer drugs, were used as therapeutic agents to kill tumors. Microbubble and iodinated x-ray contrast agents were used as imaging agents for real-time observation of microrobots under ultrasound and x-ray imaging, respectively. The magnetic actuation module, composed of electromagnetic coils, was designed to control the strength and direction of the magnetic field and allowed free movement of the microrobot in the desired direction in the 3D space. The coils of this magnetic actuation module were arranged through optimal designing, considering the clinical operational environment that may include an in vivo model, medical staff, imaging device, and microrobot injection device. In terms of microrobot targeting, the magnetic actuation modules developed to date can move microrobots only in one direction within the workspace, whereas the proposed module can generate focused magnetic fields in two points that allow microrobot movement in two directions within the workspace. The microrobot can be steered to the target vessel through two branches extending
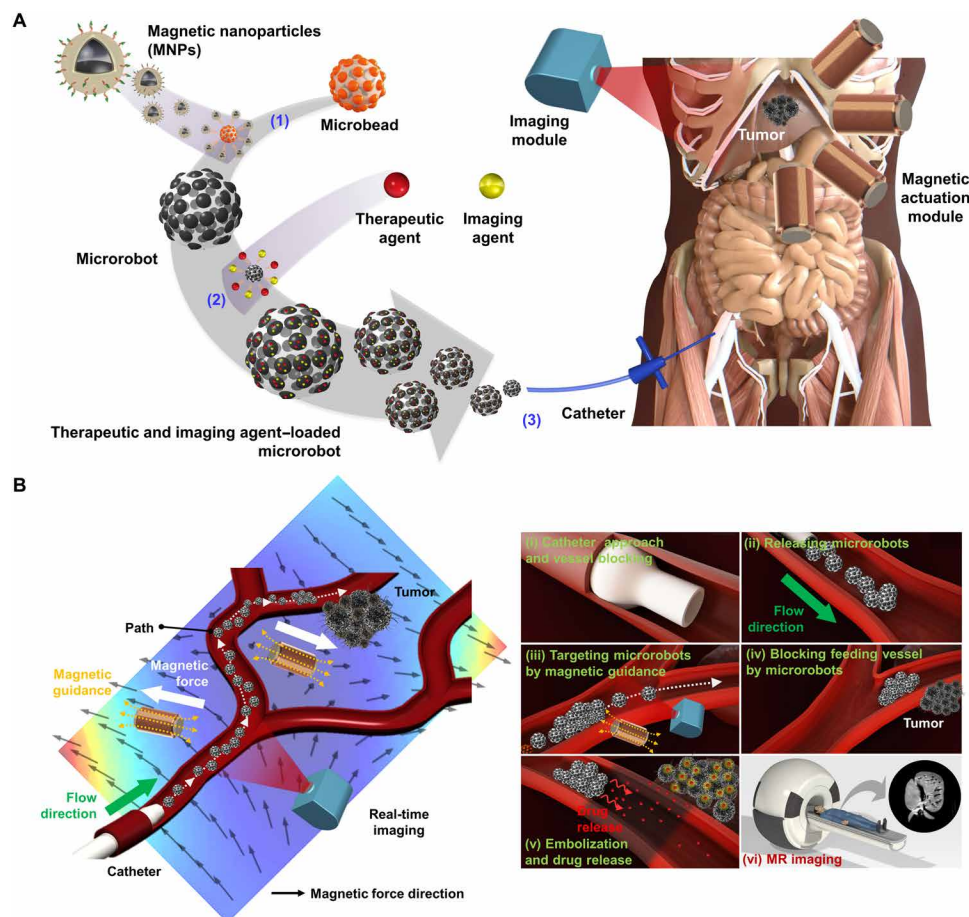
Fig. 1. Schematic of targeted vessel embolization and drug delivery using the microrobot system in vivo. (**A**) Schematic illustration of fabrication and catheter delivery of microrobots containing therapeutic and imaging agents. (1) MNPs attached on the microbead. (2) Loading of therapeutic and imaging agents on microrobots. (3) Delivery of microrobots through catheter connected to the liver vessel around the tumor. (**B**) Schematic illustration of the in vivo tumor treatment procedure using the microrobot system.

in different directions using focused magnetic fields at two points within a workspace.

Thus, with the use of multifunctional microrobots and a magnetic actuation module, we can describe the in vivo TACE procedure using the microrobot system. First, microrobots loaded with therapeutic and imaging agents are injected into a small tube of a balloon catheter that blocks blood flow along the liver vessels [(3) of Fig. 1A and (i) of Fig. 1B]. Thereafter, the microrobots are released from the catheter and guided under real-time imaging to the liver tumor feeding vessel through various branches by magnetic fields generated from the magnetic actuation module [(ii) and (iii) of Fig. 1B]. The microrobots block the feeding vessel and cause embolization [(iv) of Fig. 1B]; the therapeutic agents released from the microrobot are delivered to the tumor without affecting blood circulation and stay for a long time to inhibit or kill the tumor [(v) of Fig. 1B]. After microrobot targeting, the microrobot and tumor are then monitored through MRI [(vi) of Fig. 1B]. The targeted microrobot naturally degrades and disappears over several weeks.

On the basis of this procedure, the in vivo therapeutic effect of the microrobot system was evaluated in an orthotopic liver tumor rat model. We propose that this multifunctional medical microrobot system can reach the clinical trial phase of medical microrobots and

will make a technological leap forward to the existing embolic bead technology.

RESULTS

Fabrication and characterization of microrobots

The fabrication of the microrobot mainly consists of three steps: preparation of MNPs (Fig. 2A), formation of the microbead (Fig. 2E), and attachment of the MNPs on the surface of the microbead (Fig. 2G). MNPs were prepared by synthesizing Fe_3O_4 nanoparticles and sequential surface modification of PDA, PEG, and FA. The MNPs have the features of ease of drug loading (36), colloidal stability and stealth of the mononuclear phagocyte system (37), and folate receptor–mediated endocytosis (38), which are the advantages of PDA, PEG, and FA, respectively. The detailed process of MNP preparation is described in the Supplementary Materials (see section S2 of the Supplementary Materials). The transmission electron microscope (TEM) image of the prepared MNPs showed that the size of MNPs was approximately 12 nm (Fig. 2B), which can be easily removed by liver metabolism after microrobot biodegradation (39, 40). Energy-dispersive x-ray spectrometry (EDX) revealed the presence of C, O, N, and Fe, the major constituents of MNPs. The hydrodynamic diameter
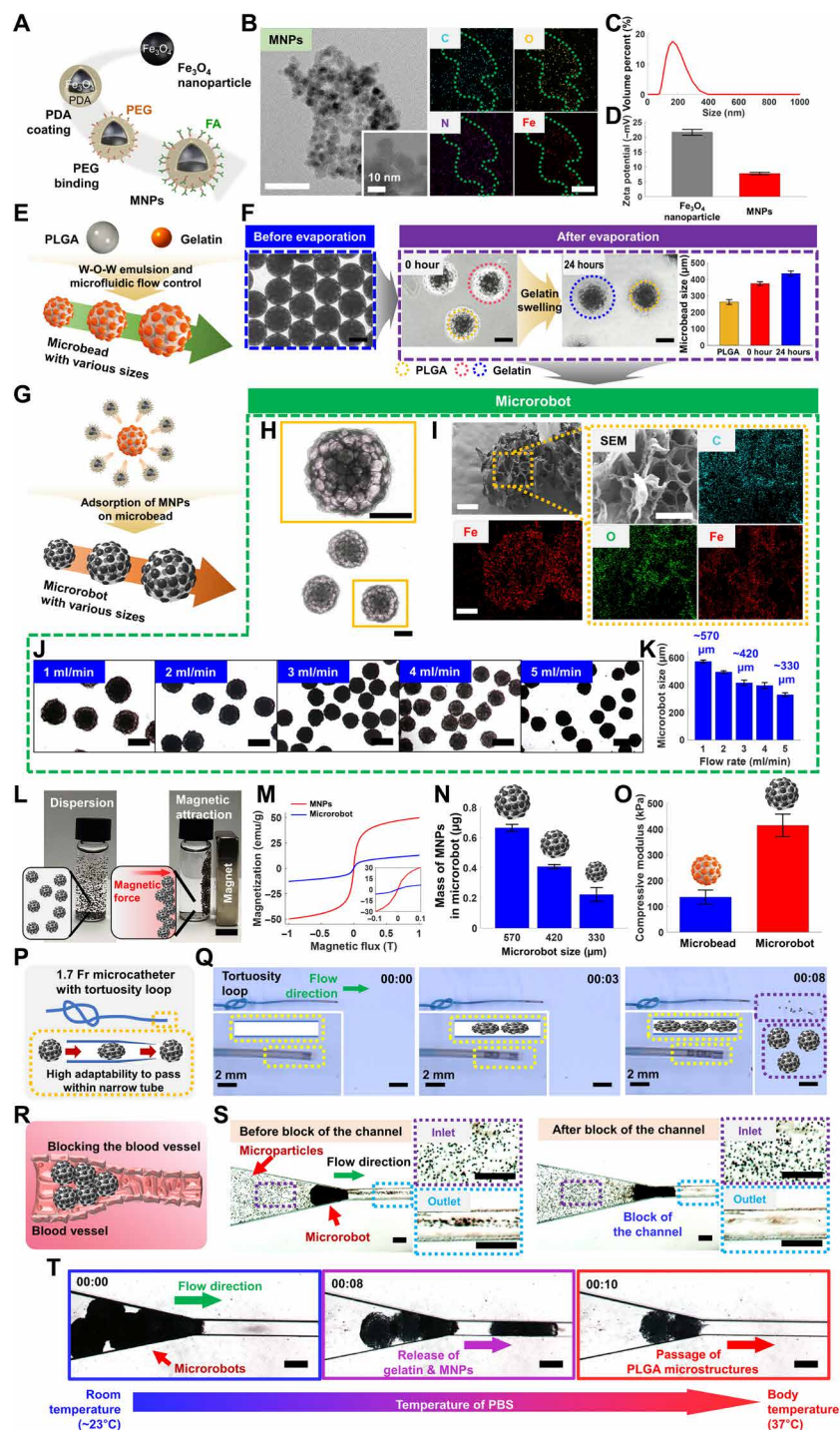
Fig. 2. Fabrication and characterization of microrobots. (**A**) Schematic illustration of the fabrication of MNPs. (**B**) TEM and EDX images of MNPs. Scale bars, 50 nm. (**C**) Size distribution of MNPs ($n = 3$; means ± SD). (**D**) Surface zeta potential of MNPs ($n = 4$; means ± SD). (**E**) Schematic illustration of the fabrication step of microbeads. (**F**) Microscopic images and graph of the microbead formation step via solvent evaporation and gelatin swelling ($n > 20$; means ± SD). The right graph shows the PLGA microstructure and microbead size before and after swelling. Scale bars, 200 μm. (**G**) Schematic illustration of the fabrication step of microrobots. (**H**) Microscopic images of the microrobots. Scale bars, 200 μm. (**I**) SEM and EDX images of the microrobot. Scale bars, 100 μm. (**J**) Microscopic images of the microrobots with different sizes. Scale bars, 500 μm. (**K**) Microrobot size at different microfluidic flow rates ($n > 15$; means ± SD). (**L**) Magnetic response of the microrobots using a magnet. Scale bar, 10 mm. (**M**) Magnetization curves of MNPs and microrobot. (**N**) Mass of MNPs in microrobots with different sizes ($n = 4$; means ± SD). (**O**) Compressive modulus of microbead and microrobot ($n = 4$; means ± SD). (**P**) Schematic illustration of microrobot delivery through a 1.7-Fr microcatheter with tortuosity loop. (**Q**) Time-lapse image sequence of microrobot delivery through a 1.7-Fr microcatheter. Scale bars, 5 mm. (**R**) Schematic illustration of the microrobot blocking the vessel. (**S**) Optical images before and after blocking the channel using the microrobots. Scale bars, 200 μm. (**T**) Time-lapse image sequence of structural change of the microrobot according to the injection of PBS at 37°C. Scale bars, 500 μm. The time is indicated on each image in the minutes:seconds format.

and surface potential (ζ) of these MNPs were approximately 165 nm (Fig. 2C) and -7.77 ± 0.4 mV (Fig. 2D), respectively. Furthermore, the characterization of MNPs using various analysis methods revealed that PDA, PEG, and FA were formed on the surface of Fe_3O_4 nanoparticles and that the magnetic-responsive properties of Fe_3O_4 nanoparticles were preserved even after several surface modifications (fig. S2 and section S4 of the Supplementary Materials). We expect that the endogenous iron metabolic pathways will decompose these MNPs into iron without toxicity in the body, and the iron released from MNPs will be metabolized by the liver (39, 40).

The microbead—microrobot body for vessel embolization, drug loading, and real-time imaging—was composed of PLGA microstructure and gelatin beads and was fabricated in the desired size using water-in-oil-in-water (w-o-w) emulsion and microfluidic flow control. For vessel embolization and drug delivery, microbeads should have sufficient structural rigidity as embolic beads, and it should be easy to load and release drugs using them. Therefore, we optimized the concentration and ratio of PLGA and gelatin in w-o-w emulsion to stably form microbeads from gelatin beads and PLGA porous microstructure (figs. S3 to S6 and section S5 of the Supplementary Materials). Thus, for w-o-w emulsion bead formation by microfluidic flow, the optimized ratio of PLGA and gelatin was 5.5:4.5, and the concentrations of PLGA and gelatin were 75 mg/ml and 10%, respectively. Thereafter, emulsion beads were converted into microbeads with the PLGA porous microstructure through solidification by PLGA solvent evaporation (Fig. 2F and see movie S1). After solidification, the gelatin beads of the microbeads were allowed to swell for 24 hours to maintain equilibrium with the immersed solution. The microbeads formed with a fluid flow of 3 ml/min had a diameter of approximately 435 µm, which included a PLGA porous microstructure with a diameter of 260 µm (graph of Fig. 2F). We confirmed that microbeads with diameters from 287 to 560 µm can be obtained, including PLGA porous microstructures with diameters from 151 to 390 µm, by controlling the microfluidic flow from 1 to 6 ml/min (fig. S7, A, B, and D). Furthermore, we obtained small-sized microrobots (168 µm) at a fluidic flow of 6 ml/min and a PLGA:gelatin ratio of 6:4 (fig. S7, E and F). Thus, on the basis of the location of the liver tumor, the size and shape of the feeding vessel can be determined, and microbeads of appropriate size can be selected from the wide range of sizes of microbeads, similar to commercial embolic beads of various sizes (100 to 1000 µm) (27, 28, 41).

The microrobot was fabricated by attaching MNPs to the surface of the microbead for magnetic actuation and MRI (Fig. 2G). Specifically, MNPs were attached to the microbead because of the reaction between catechols of PDA on MNPs and amines of gelatin on the microbead (42). In addition, the electrostatic interaction between the surface electric charges of MNPs and gelatin is attributed to the attachment of MNPs on the microbead. An optical microscope image showed that the diameter of the microrobot using microbeads formed at a fluid flow of 3 ml/min was approximately 420 µm (Fig. 2H). The EDX analysis image showed that the microrobot contained C and O, which are the main components of microbeads, as well as Fe, which is a major component of MNPs (Fig. 2I). In addition, we could fabricate microrobots with diameters ranging from 300 to 570 µm by attaching MNPs to microbeads obtained through microfluidic flow control (Fig. 2, J and K, and fig. S7, C and D). Thermal gravimetric analysis curve and Fourier transform infrared (FTIR) spectra of the microrobot and its major components showed weight loss curves and IR absorbance bands corresponding to MNPs,

PLGA, and gelatin. These results indicate that both microbeads and MNPs, which are the components of microrobots, exist even after several fabrication processes (fig. S8, A and B, and section S6 of the Supplementary Materials). The magnetic-responsive properties of the microrobots were observed as strong attraction to the magnets to the dispersed microrobots when brought close to them (Fig. 2L). In addition, the magnetization curve of the microrobots and MNPs shows that the magnetization saturation of the microrobots (approximately 13 emu/g) was 3.8 times lower than that of MNPs (approximately 50 emu/g) (Fig. 2M), implying that the microbead occupies approximately 74% of the total mass of the microrobot. Furthermore, the mass of each MNP contained in microrobots of various sizes was calculated using inductively coupled plasma optical emission spectroscopy. When the measured concentration of Fe in MNPs was 71% (fig. S8C), the masses of MNPs in one microrobot with diameters of 570, 420, and 330 µm were 0.66, 0.41, and 0.22 µg, respectively (Fig. 2N). These results indicate that the amount of MNPs attached to the microrobot depends on the size of the microrobot.

The mechanical properties of the embolic bead are essential for determining the embolization behavior. Among the mechanical properties of the embolic bead, elasticity should be measured because it indicates the ability to recover its original size after injection with a microcatheter. We performed the microrobot compression test (fig. S8D) and found that the microrobot's compressive modulus (414.4 kPa) is higher than that of the microbead (135.8 kPa) (Fig. 2O). We hypothesize that the compressive modulus of the microrobot is influenced by a reaction between gelatin and MNPs on the surface of the microrobot. Furthermore, to confirm the compatibility of microrobots with commercial catheters, microrobot delivery was performed using catheters of various sizes (movie S2). All microrobots of different sizes could be delivered through catheters with diameters of 4.0 Fr (inner diameter: 33 mm) and 2.4 Fr (inner diameter: 0.79 mm). In addition, microrobots could be delivered through a microcatheter with a small diameter (1.7 Fr; inner diameter: 0.43 mm) because of the high elasticity of microrobots. Moreover, we observed microrobot delivery in a microcatheter with a tortuosity loop to mimic a microcatheter connected along a complex blood vessel (Fig. 2P) (43). The results indicated that the compressed microrobot can recover its original shape after passing through and coming out of the narrow and twisted tube (Fig. 2Q).

Before the phantom and in vivo experiments, the occlusion of microrobots was tested in straight microfluidic channels of different widths (Fig. 2R). Microrobots of various sizes passed through channels with widths of 600 and 300 µm, which were smaller than those of microrobots (movie S3). On the other hand, all microrobots were sequentially stacked in a channel with a width of 150 µm and consequently blocked the channel. Microparticles of 5 µm did not pass through the channel completely blocked by the microrobot (Fig. 2S and movie S3). Considering that the size of red blood cells that transport oxygen through hemoglobin is about 7 µm (44), it suggests that microrobot vessel occlusion can not only block oxygen delivered to the tumor but also reduce nutrients due to decreased blood flow. Also, considering that the hepatic capillary and microcirculation sizes are 5 and 100 µm, respectively (45), the microrobot occludes the vessel before delivery to the hepatic microcirculation. In addition, the structural behavior of the microrobot according to temperature was observed in the fluidic channel occluded by the microrobot to examine the microrobot change after vessel embolization. The flow of phosphate-buffered saline (PBS) above 37°C, which is the blood temperature,

in the fluidic channel occluded by the microrobot caused the release of gelatin and MNPs because of the low melting point of gelatin (Fig. 2T and movie S4). Thereafter, the PLGA microstructure, which is smaller than the microrobot, could pass through the channel. These experimental results are somewhat exaggerated but reveal that gelatin and MNPs can be released from the microrobot in the body, and the remaining PLGA microstructure can continue to function as an embolic bead.

In vitro biocompatibility, thrombogenicity, and biodegradability of microrobots

The in vitro biocompatibility and biodegradability of microrobots were investigated through cell viability and degradation tests. To confirm the biocompatibility of MNPs, the cell viability of human umbilical vein endothelial cells (HUVECs), human aortic endothelial cells (HAECs), and normal human liver epithelial cells or endothelial and epithelial (THLE-2) cells was tested at different concentrations of MNPs (Fig. 3A). The viability of HUVECs and HAECs decreased at an MNP concentration of ≥30 µg/ml (Fig. 3, B and C), whereas that of THLE-2 cells was not significantly affected at an MNP concentration of ≥50 µg/ml (Fig. 3D). Furthermore, the cell viability of HUVEC, HAEC, THLE-2, and human hepatoma cells (Hep3B) was tested using 100 microrobots (Fig. 3E). In addition, the cell viability of HUVECs, HAECs, THLE-2 cells, and Hep3B cells was evaluated using 100 microrobots (Fig. 3E). No significant difference in cell viability was found between the control group (cells incubated without microrobots) and the test group (cells incubated with 100 microrobots for 48 hours) (Fig. 3F). Considering that 100 microrobots contained approximately 66 µg of MNPs, we hypothesized that cell viability would be higher when MNPs were slowly released from microrobots than during treatment with MNPs alone. Furthermore, the hemocompatibility of MNPs and microrobots was investigated by analyzing hemolysis of red blood cells following treatment with MNPs and microrobots (46). The surfactant triton-induced hemolysis of red blood cells produced hemoglobin, which was dark red in color, and absorption of the supernatant at 590 nm was high (Fig. 3G and fig. S9). On the other hand, despite the treatment with various concentrations of MNPs and microrobots, hemoglobin was hardly produced by hemolysis of red blood cells, as revealed by the transparency of the supernatant and no change in absorption intensity (fig. S9). Hence, we confirmed that the microrobots had no toxic effect on red blood cells.

Thrombogenicity, which indicates the tendency of a substance to cause thrombosis or clotting when in direct contact with blood, is one of the important biological properties in the evaluation of embolic agents. We evaluated the thrombogenicity of microrobots using sheep blood in 96-well plates (Fig. 3H) (34, 35). Coagulation of blood (control) started after 9 min, whereas coagulation occurred around the microrobots from 5 min after contact (Fig. 3I). In addition, we confirmed that the blood in contact with the microrobots produced more blood clots than the control at 13 min through the darker color. These results indicate that microrobots can promote blood coagulation and thus function as an embolic agent.

To use the proposed microrobots for vessel embolization, their biodegradability should be ensured to avoid side effects caused by untargeted microrobots. PLGA and gelatin, the major components of the microrobot, are known to be degraded in vivo by hydrolysis and enzyme of matrix metalloproteinase–sensitive protein sequences, respectively (47, 48). In addition, gelatin has a melting point of

approximately 35°C and is also removed by phagocytosis (49, 50). Hence, after targeted vessel embolization by the microrobot, gelatin beads of the microrobot induce thrombus formation and gradually degrade through a foreign body reaction at the blood temperature. The PLGA microstructure, which has a longer degradation period than gelatin, degrades slowly over several weeks even after the gelatin disappears. To verify this, we monitored the in vitro degradation of the microrobot using an optical camera and scanning electron microscope (SEM) during culturing in PBS for 49 days (Fig. 3J). On the first day, optical and SEM images showed that gelatin and MNPs were released from the microrobot, and the presence of C and O in EDX analysis revealed that only the PLGA microstructure with few MNPs remained (Fig. 3, K and L). After 21 days, the morphology of the PLGA microstructure collapsed because of hydrolysis, and on the 49th day, the PLGA microstructure was degraded into several fragments (Fig. 3M).

Imaging agent–loaded microrobots enabled real-time and postoperative imaging

To track the targeting of microrobots in real time, we selected x-ray and ultrasound-based imaging methods, which are most commonly used for observing deep tissues such as vessels, the liver, and kidneys. Thus, for real-time imaging of microrobots using ultrasound and x-ray, the microrobots should be composed of a material that can be detected by ultrasound or x-ray or be loaded with contrast agents for that imaging. In this study, we loaded contrast agents into the microrobots to develop multifunctional microrobots, i.e., microrobots that enabled magnetic actuation, drug delivery, and real-time and postoperative imaging.

Ultrasound imaging of the microrobots was performed by loading them with SONAZOID (GE Healthcare, Waukesha, WI, USA), a microbubble contrast agent (Fig. 4A). SONAZOID, approved in many countries as an ultrasound imaging agent, is composed of lipid-coated perfluorocarbon microbubbles measuring approximately 3 µm and is mainly used for imaging liver and breast lesions (51). Microbubbles disappear approximately 10 min after injection, and the gas is removed from the body by exhalation. The absorbance intensity of microbubbles at various concentrations in PBS was measured at 660 nm (Fig. 4B). The mass of microbubbles loaded in the microrobots was measured using the intensities measured at each concentration. Each microrobot contained approximately 2.22 µg of microbubbles (Fig. 4C). Thereafter, real-time imaging of the microbubble-loaded microrobots was performed in a tube. The microrobots were observed freely moving in a swarm motion in the tube under magnetic field influence by real-time ultrasound imaging (Fig. 4D).

An iodinated contrast agent is most frequently used clinically to visualize internal vessels; however, this agent can cause damage to blood vessels and kidneys if it remains in the body for a long period of time. We needed to use an iodinated contrast agent to enable real-time x-ray imaging of the microrobots (Fig. 4E) and conducted several experiments to observe the loading and release of the iodinated contrast agent from them. The change in the iodine content of microrobots with a diameter of 570 µm was investigated through EDX (Fig. 4F). We found that their iodine content was 10.29% after loading the agent and that it was only 1.32% after releasing in PBS for 1 day. In microrobots with a diameter of 420 and 330 µm, the iodine content after loading the agent was 6.67 and 4.16%, respectively, which corresponded to the smaller volume of these microrobots compared with microrobots with a diameter of 570 µm. After release,
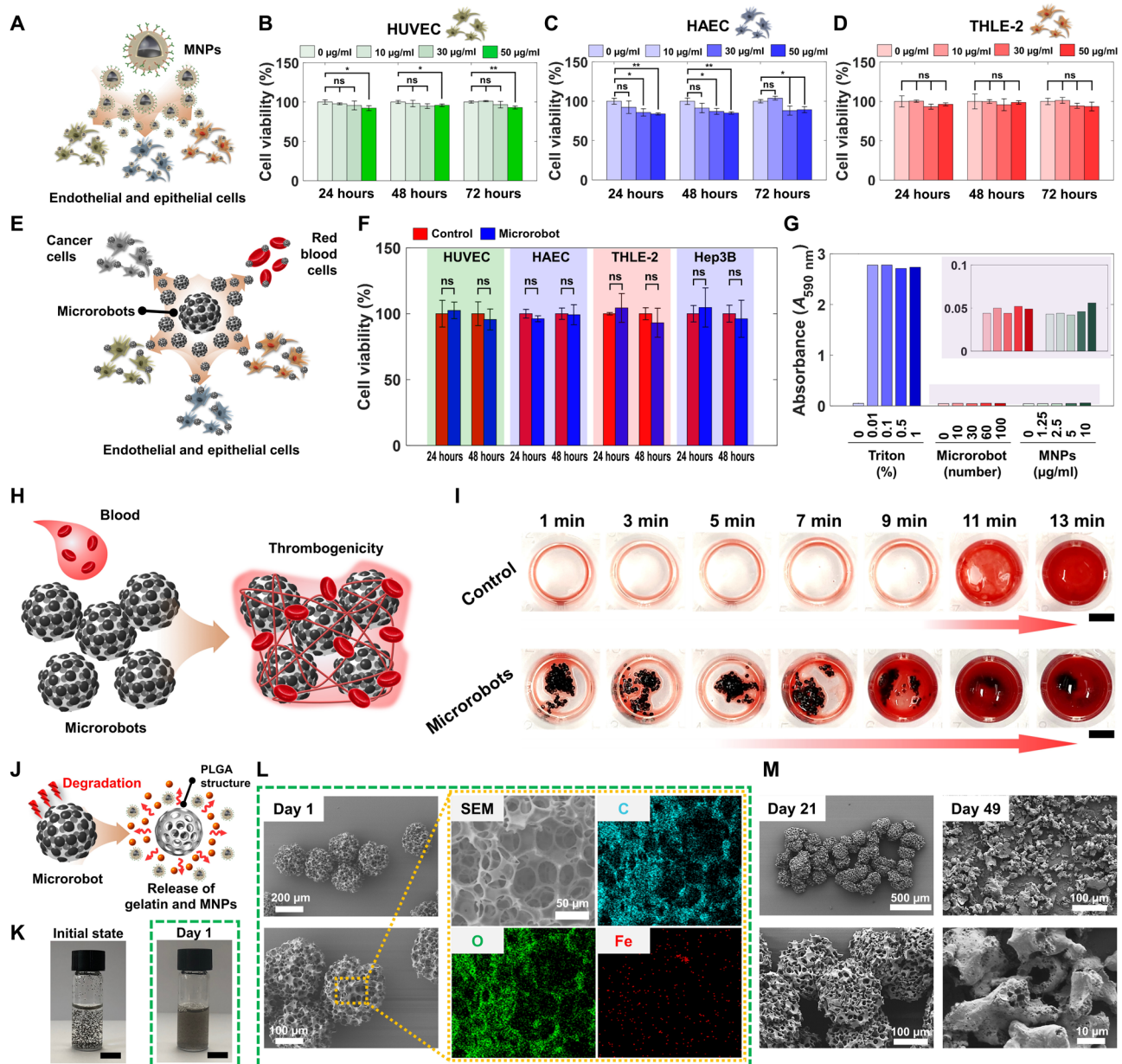
Fig. 3. Microrobots do not have a cytotoxic effect and degrade gradually over time. (**A**) Schematic illustration of the biocompatibility of MNPs to cells. (**B** to **D**) Cytotoxicity of MNPs in (B) HUVECs, (C) HAECs, and (D) THLE-2 cells for 72 hours ($n = 3$; means ± SD, *$P < 0.05$ and **$P < 0.01$, Student's t test). ns, not significant. (**E**) Schematic illustration of the biocompatibility of microrobots to cells. (**F**) Cytotoxicity of microrobots in HUVECs, HAECs, THLE-2 cells, and Hep3B cells for 48 hours ($n = 3$; means ± SD, Student's t test). (**G**) Hemocompatibility of MNPs and microrobots. Absorption of supernatants of the red blood cell solution was measured at 590 nm. (**H**) Schematic illustration of microrobot thrombogenicity. (**I**) Thrombogenicity assay showing the clotting time of the microrobot in contact with sheep blood. Blood alone was used as a negative control. Red arrows indicate the progression of thrombus formation. Scale bars, 3 mm. (**J**) Schematic illustration of microrobot degradation. (**K**) Optical images of microrobots immersed in PBS at initial state and day 1. Scale bars, 10 mm. (**L**) SEM and EDX images of microrobots immersed in PBS at day 1. (**M**) SEM images of microrobots after degradation in PBS at day 21 (left) and day 49 (right).

the iodine content in these microrobots was 2.78 and 1.80%, respectively. These results indicate that most of the iodinated contrast agent is rapidly released from the microrobots, and only a small amount remains in the body. Real-time monitoring of the iodinated contrast agent–loaded microrobot was performed under x-ray irradiation. Microrobots immersed in PBS could be visualized in real time (Fig. 4G, fig. S10, and movie S5). Over time, the iodinated contrast

agent was released, making the microrobot further blurry and eventually invisible on x-ray imaging. The real-time x-ray imaging durations for microrobots with diameters of 570, 420, and 330 μm were 65, 35, and 25 s, respectively (Fig. 4H and fig. S10). This trend was observed because of the difference in the amount of iodinated contrast agent loaded in the microrobot, which is associated with the microrobot size. Although real-time imaging of microrobots is possible
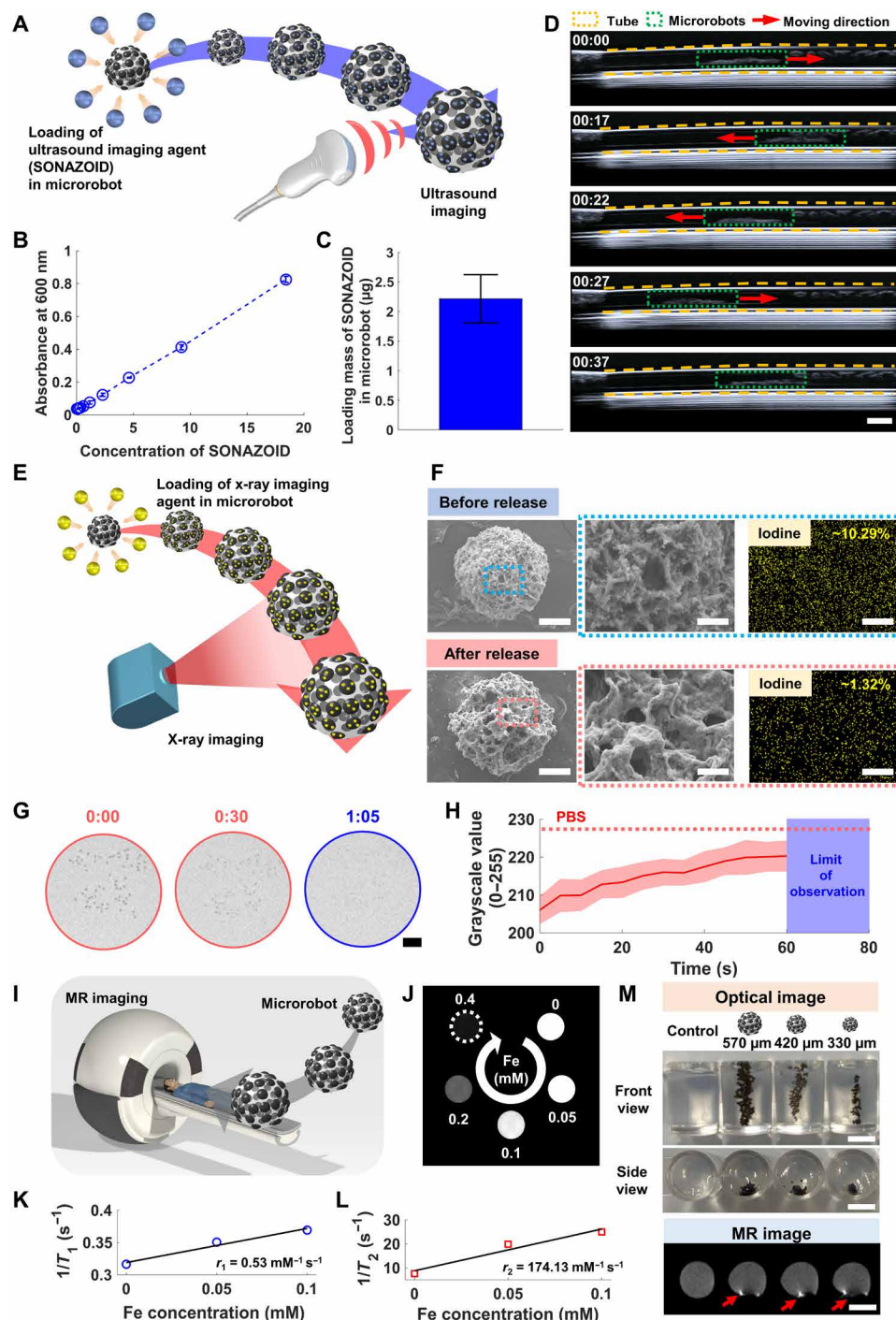
Fig. 4. Microrobots containing imaging contrast agents enable real-time (ultrasound and x-ray) and postoperative MRI. (**A**) Schematic illustration of ultrasound imaging of ultrasound contrast agent (SONAZOID)–loaded microrobots. (**B**) Standard curve of the ultrasound contrast agent according to concentration ($n = 3$; means ± SD). (**C**) Loading mass of SONAZOID in microrobots with a diameter of 570 μm ($n = 3$; means ± SD). (**D**) Time-lapse image sequence of SONAZOID-loaded microrobot movement under ultrasound guidance. Scale bar, 4 mm. (**E**) Schematic illustration of x-ray imaging of iodinated contrast agent–loaded microrobots. (**F**) SEM and EDX images of microrobots with a diameter of 570 μm before and after release of the iodinated contrast agent in PBS for 24 hours. Scale bars [on SEM (left) and SEM/EDX (right)], 100 and 25 μm, respectively. (**G**) Time-lapse image sequence of the movement of iodinated contrast agent–loaded microrobots with a diameter of 570 μm under x-ray guidance. Scale bar, 3 mm. (**H**) Change in grayscale values of iodinated contrast agent–loaded microrobots with a diameter of 570 μm on x-ray imaging ($n > 25$; means ± SD). (**I**) Schematic illustration of MRI of microrobot. (**J**) T_2-weighted MR image of MNPs in aqueous solutions of different Fe concentrations. (**K**) Relaxation rate r_1 ($1/T_1$) of MNPs at different Fe concentrations ($n = 3$; means ± SD). (**L**) Relaxation rate r_2 ($1/T_2$) of MNPs at different Fe concentrations ($n = 3$; means ± SD). (**M**) Optical and MRI of microrobots of different sizes in the phantom. Scale bars, 5 mm. The time indicated on each image is in the minutes:seconds format.

for only tens of seconds, the time for microrobot targeting is just a few seconds; thus, the real-time imaging duration of the proposed microrobots is sufficient for tracking them during and after targeting.

After microrobot delivery to the target tumor feeding vessel, their biodistribution and tumor treatment efficacy should be noninvasively monitored through postoperative imaging. In this study, we selected MRI as the postoperative imaging method for observation of the targeted microrobots and tumor status (Fig. 4I). MNPs with an Fe_3O_4 core (loaded on the microrobots) are negative contrast agents for MRI, and their signal intensity can be changed by shortening the transverse relaxation time (T_2) of water protons (52). Within the uniform magnetic field generated by the MRI scanner, the gradient magnetic field is close to zero, and as a result, the MNP-loaded microrobots delivered to the lesion site are not driven during MRI acquisition. Food and Drug Administration–approved MNPs are already being used as MRI contrast agents. They are administered orally or intravenously and circulate throughout the body. Hence, the MNPs loaded on microrobots improve the visibility of internal structures in the body in MR images without affecting microrobot magnetic actuation (53, 54). MRI revealed that the developed MNPs could generate negative contrast by changing the signal intensity with Fe concentration on MRI (Fig. 4J). Both the T_1 relaxation rate ($1/T_1$) and T_2 relaxation rate ($1/T_2$) had a positive linear relationship with the Fe concentration. The r_1 value (0.53 mM^{-1} s^{-1}) for the Fe concentration in MNPs was lower than that for gadolinium-based T_1 contrast agents (4 to 5 mM^{-1} s^{-1}) (Fig. 4K) (55), whereas the r_2 value (174.13 mM^{-1} s^{-1}) of the Fe concentration in MNPs was similar to that of commercial MNP–based T_1 contrast agents (120 to 186 mM^{-1} s^{-1}) (Fig. 4L) (52). These results mean that fabricated MNPs can be used as a negative contrast agent for MRI. Furthermore, we observed MR images of microrobots containing MNPs in the prepared phantom (Fig. 4M). Optical and T_2-weighted images showed that 100 microrobots with diameters of 570, 420, and 330 μm in each phantom can be observed by MRI.

Tumor treatment effect of therapeutic agent–loaded microrobots in vitro

In this study, the drug was loaded onto gelatin beads and MNPs, which are the main components of the microrobot, and we designed the drug to be pH-sensitively released from the microrobot according to the acidic environment around and inside the tumor. First, drug-loaded MNPs are released from the microrobot located in the blood vessels around the tumor as the microrobot degrades. Some of these MNPs have the potential for uptake into tumor cells by entering endosomes and lysosomes (56), which have an acidic environment of about pH 5.0 (57). Next, the drug loaded on the gelatin beads is slowly released from the microrobot. Here, some microrobots located close to or inside the tumor tissue are exposed to the acidic microenvironment of the tumor at a pH of about 5.0 (58). To verify the pH-sensitive drug release and in vitro tumor treatment effects of drug-loaded microrobots, we performed drug loading and release tests and in vitro cancer cell viability tests.

We examined the drug loading capacity and cancer cell uptake of MNPs, a component of microrobots. DOX, a representative anticancer drug, was loaded on MNPs. DOX was loaded on the PDA of MNPs by π-π stacking and hydrogen bonding interactions. The drug loading capacity of MNPs was up to 25%, depending on the ratio of MNPs to DOX (fig. S11A). The drug release behavior of DOX-loaded MNPs was observed at pH 5.0 and pH 7.4, where pH 5.0 and pH 7.4

are similar to intracellular endosome and lysosome and physiological environment, respectively (57). The amount of DOX released from the microrobot was 14.3 and 6.1% at pH 5.0 and pH 7.4 for 24 hours, respectively. The amount of DOX released at pH 5.0 was more than twice that at pH 7.4 (fig. S11B). The higher release of DOX at low pH may be because of the high positive charge resulting from the protonation of DOX molecules at low pH (59). FA-induced folate receptor–mediated endocytosis of MNPs was observed in Hep3B and THLE-2 cells in various conditions using fluorescence imaging. In Hep3B cells, a human liver tumor cell, free DOX, is distributed throughout the cell, including the nucleus, by direct cell infiltration of DOX molecules with a diameter of approximately 1.5 nm (56). On the other hand, DOX-loaded MNPs enter the endosome and lysosome in the cell through endocytosis (56). Thereafter, DOX is rapidly released from MNPs in the acidic environment of the endosome and lysosome. The fluorescence image of the DOX-loaded MNP group showed that DOX released from the endosome and lysosome was trapped inside the cell in the perinuclear cytoplasm (fig. S11C, left). The blocking of folate receptors of cells by FA treatment resulted in relatively low DOX fluorescence, which indicated that endocytosis of MNPs into cells was reduced because of folate receptor blocking. Furthermore, in THLE-2 cells, MNP uptake was found to be low, regardless of FA treatment, as revealed by low DOX fluorescence intensity (fig. S11C, right). This phenomenon proves that the folate receptor is overexpressed in cancer cells compared with normal cells. Hence, MNPs released after the degradation of microrobots have the potential to be used as secondary drug carriers for effective drug delivery through uptake into tumors.

The drug was loaded into the microrobots through absorption of DOX and 5-FU aqueous solution, which are frequently used as chemotherapeutic agents in tumor treatment, into the gelatin beads of the microrobot (Fig. 5A). Optical and fluorescence images showed that DOX can be loaded into microrobots of various sizes (Fig. 5B). The amounts of DOX and 5-FU loaded into the microrobot were determined according to the size of the microrobot (Fig. 5C). Microrobots with a diameter of 570, 420, and 330 μm contained 0.95, 0.32, and 0.16 μg of DOX, respectively. Furthermore, each microrobot with a diameter of 570, 420, and 330 μm contained 0.23, 0.11, and 0.09 μg of 5-FU. In the drug loading process, the concentration of the aqueous solution of DOX (50 mg/ml) was higher than that of 5-FU (16 mg/ml); hence, more DOX was loaded into the gelatin beads of the microrobots. In addition, DOX can react with the PDA of MNPs, which is a component of the microrobots, and therefore, additional drugs can be loaded into the microrobots. Furthermore, drug release from the microrobots was observed in PBS at pH 5.0 and 7.4, which corresponded to the acidic microenvironment of the tumor and physiological environment, respectively (Fig. 5D) (58). The amounts of DOX and 5-FU released from the microrobots at pH 7.4 were 53.9 and 69.2% and those released at pH 5.0 were 93.1 and 92.2%, respectively, within 24 hours (Fig. 5, E and F). We hypothesized that protonation of drugs at low pH may have facilitated drug release from microrobots (59, 60). The validation of tumor treatment with drug-loaded microrobots was performed in vitro using Hep3B cells, a liver cancer cell (Fig. 5G). Compared with the high viability in control (only cells) and 100 microrobots without drug, 100 microrobots loaded with DOX and 5-FU could kill cancer cells with low viability (DOX- and 5-FU–loaded microrobots: 28.5 and 42.3%, respectively) (Fig. 5, H and I). In addition, the cancer cell
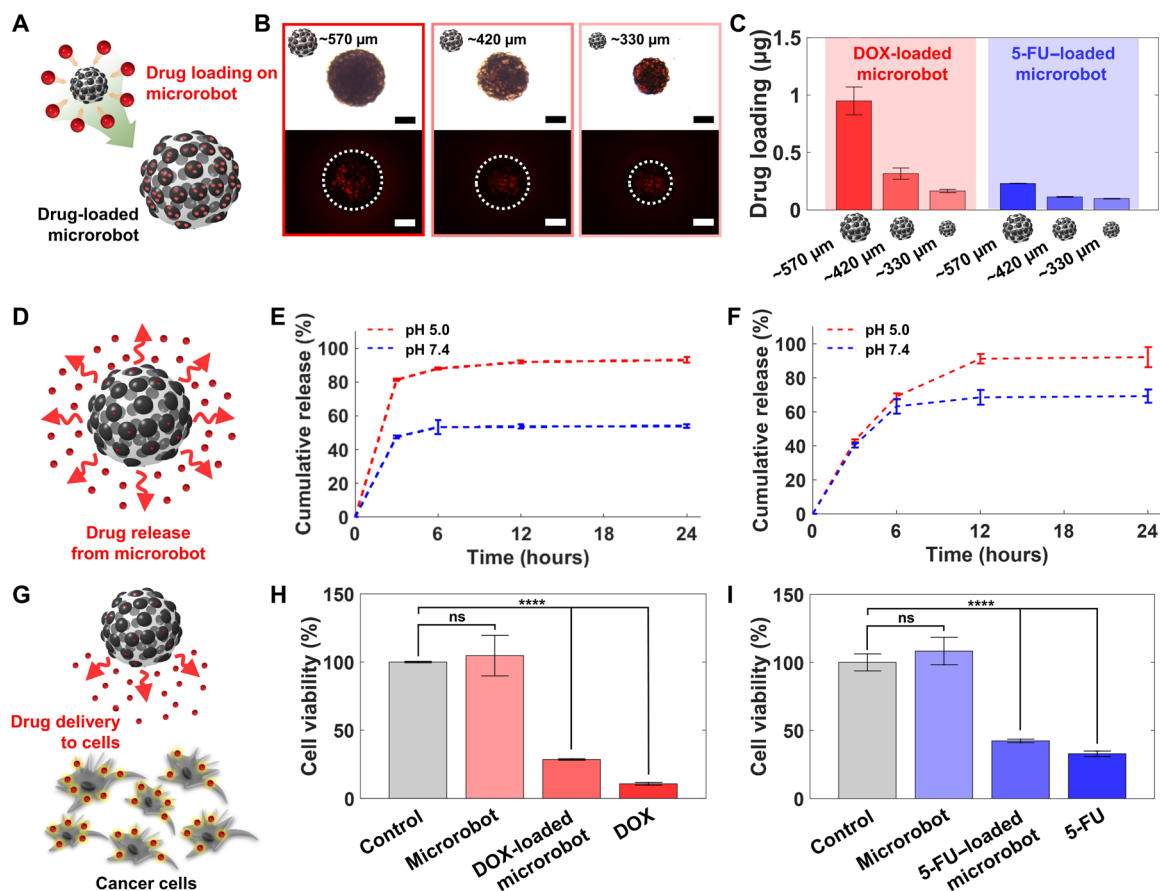
Fig. 5. Loading and release of therapeutic agents (DOX and 5-FU) from microrobots for the treatment of cancer cells. (**A**) Schematic illustration of the drug-loaded microrobot. (**B**) Optical and fluorescence images of DOX-loaded microrobots of different sizes. Scale bars, 200 μm. (**C**) Mass of DOX and 5-FU loaded in one microrobot with different sizes. (**D**) Schematic illustration of drug release from the microrobot. (**E**) DOX and (**F**) 5-FU release from a microrobot with a diameter of 570 μm in buffer at pH 5.0 and 7.4 ($n = 3$; means ± SD). (**G**) Schematic illustration of drug delivery to cells using microrobots. (**H** and **I**) Viability of Hep3B cells after treatment with microrobots, drug-loaded microrobots, and drug at 24 hours. Cell viability after treatment with free and microrobot-bound (H) DOX and (I) 5-FU ($n = 3$; means ± SD, ****$P < 0.0001$, Student's t test).

viability of cells treated with free DOX and 5-FU was lower (DOX and 5-FU: 10.7 and 32.9%, respectively) than that of cells treated with drug-loaded microrobots. This difference is because of the drug delivery method of microrobots. Free DOX and 5-FU immediately diffuse into the culture media as an aqueous solution and penetrate the cell directly, but drugs loaded in the microrobot are slowly released and diffused into the cell. Furthermore, considering the in vitro and in vivo environment with respect to drug delivery, the in vitro environment is an isolated system in which drug concentration is maintained, unlike the in vivo environment. In the in vivo environment, the drug spreads throughout the body because of blood circulation and kills tumor and normal tissues. On the other hand, the microrobot targeted to the tumor feeding vessel blocks the blood flow, gradually releases the drug, and stays around the tumor for a long time, thereby enhancing the tumor treatment effect.

We investigated the near-IR–triggered heat generation ability of microrobots, which is an additional function of the proposed microrobot. The response of microrobots to NIR can be induced by PDA, a component of MNPs. PDA has the property of NIR absorption (808 nm) (fig. S2C) and is known to induce a photothermal effect through high photothermal conversion efficiency (61). NIR irradiation

(2 W/cm², 1 min) increased the temperature of PBS even in the presence of only one microrobot (fig. S12, A and B). An increase in the number of microrobots increased the temperature remarkably. In addition, the increase in the temperature of the microrobots due to NIR irradiation caused the release of MNPs and gelatin from the microrobots (fig. S12C). Hence, we anticipate that NIR-triggered heat generation will enable controlled drug release and promote the release of gelatin and MNPs from microrobots.

Validation of targeting, real-time x-ray imaging, and embolization of microrobots using a magnetic actuation module in the vessel phantom model

To deliver microrobots to the target tumor feeding vessel, we used a magnetic actuation module consisting of multiple electromagnetic coils. The configuration of electromagnetic coils in the magnetic actuation module was designed considering targeting with an in vivo microrobot injection and real-time imaging; thus, the magnetic actuation module provided access to animals, respiratory anesthesia equipment, microrobot injection device, x-ray imaging device, and operator (fig. S13 and see section S8). In addition, for targeting of microrobots in complex narrow blood vessels in the body, the

magnetic actuation module was designed to implement five (two rotational and three translational) degree-of-freedom motions. The fabricated magnetic actuation module comprised nine electromagnetic coils that were placed in the upper and lower regions. Detailed configuration and specifications of the magnetic actuation module are described in fig. S14 and tables S1 and S2. The configuration of these coils enabled targeted vessel delivery of microrobots under x-ray guidance without interference of animals, respiratory anesthesia equipment, microrobot injection devices, and x-ray imaging devices. The fabricated magnetic actuation module can simultaneously generate a magnetic field of 70 mT and a gradient magnetic field of 1.7 T/m.

Before targeted vessel delivery using microrobots in the vessel phantom, the mobility of the microrobot under the magnetic field in PBS and blood was evaluated through numerical simulation and measurement (see section S9). First, we set up a model based on the finite element method for numerical simulation of the moving speed of the microrobot (Fig. 6A). Considering that the microrobot moves at a constant velocity when the sum of the magnetic force and drag force becomes 0, the numerical analysis of the microrobot speed was performed, and the microrobot speed was calculated until the drag force acting on the microrobots became ≥95% of the magnetic force (Fig. 6B). Simulation results revealed that in a magnetic field of 40 mT and a gradient magnetic field of 1 T/m, the maximum speeds of the microrobots in PBS and blood were 1.53 and 0.32 mm/s, respectively, and the minimum speeds of the microrobots in PBS and blood were 0.84 and 0.2 mm/s, respectively; minimum and maximum speeds of the microrobots varied with the microrobot size (Fig. 6C). In the speed value in blood, the Reynolds number of the microrobots was <0.05, corresponding to the Stokes flow (Fig. 6D and fig. S15A). In addition, in a magnetic field of 40 mT and a gradient magnetic field of 0.5 T/m, the speed of the microrobots was reduced by half of 1 T/m because the magnetic force was proportional to the gradient magnetic field (fig. S15B). Furthermore, the microrobot speed was measured in PBS and 10% fetal bovine serum (4.2 centipoise), with a viscosity similar to blood (Fig. 6C). We found that the simulated and measured speeds of microrobots were similar, as revealed by the simulated and measured values.

To show the targeted vessel embolization using microrobots, the phantom was designed to have two branches. The diameter of the two branches was set on the basis of the branches that are maximally accessible to the 1.4-Fr microcatheter (fig. S16) (27). Figure 6E shows the experimental setup for targeted vessel embolization using microrobots. Before microrobot targeting in the vessel phantom, we investigated whether the magnetic actuation module could generate a magnetic force to target each vessel of the phantom through numerical simulation. In the set-up stage of the numerical simulation of the magnetic actuation module (fig. S17), the strength and direction of the magnetic force were set differently for the current applied to each electromagnetic coil according to the target vessel. The simulation results revealed that a strong magnetic field can be formed at two points, and the microrobot can be magnetically guided to the target vessel through the two branches (Fig. 6, F to I). In addition, both the strength and direction of the generated magnetic force were directed to each target vessel of the phantom. These results suggest that microrobots can be directed to the target vessel under magnetic guidance using the magnetic actuation module.

On the basis of the simulation results, we performed targeted vessel embolization using microrobots in the phantom under observation of optical and x-ray imaging. The microrobots were magnetically steered to the targeted area using a magnetic field of 40 mT and a gradient magnetic field of 1 T/m. Optical and x-ray images revealed that iodinated x-ray contrast agent–loaded microrobots in the phantom can be monitored with real-time x-ray imaging (Fig. 6, J to N, fig. S18, and movie S6). Most of the microrobots were delivered to each of the four target vessels under magnetic guidance compared with no magnetic guidance. Quantitatively, in the absence of magnetic guidance, almost the same number of microrobots (approximately 50%) were stacked in the left and right vessels of the first branch (Fig. 6O). On the other hand, with the use of magnetic guidance, at least 92% (average of targeting efficiency in Fig. 6, P to S) of microrobots were delivered to the target vessel of the first branch, and at least 63% (average of targeting efficiency in Fig. 6, P to S) were delivered to the target vessel of the second branch (Fig. 6, P to S). We hypothesized that the lowered targeting efficiency in the second branch was caused by the error in the strength and direction of the magnetic field generated by the magnetic actuation module. In addition, we determined the fluid flow after channel blockage by microrobots. The microrobot speed was reduced to 2.26, 1.68, and 0.79 mm/s as the right and left vessels of the second branch were sequentially blocked by microrobots (Fig. 6T and movie S7). Furthermore, target vessel embolization was analyzed by using change in the x-ray contrast at one point of each vessel of the second branch according to the injection of iodinated x-ray contrast agent (Fig. 6, K to N, dotted circles in x-ray images). On the basis of the grayscale values of PBS (>215.8) and x-ray contrast agent (>193.8) on the x-ray image (fig. S19), all grayscale values were higher in the vessel to which microrobots were delivered (Fig. 6, U to X). These results indicate that the microrobot can be delivered to the target vessel under magnetic guidance and can block the fluid flow through vessel embolization.

In vivo validation of targeted vessel embolization and degradation of microrobots

In vivo targeted vessel embolization was performed in the rat liver using the microrobot system. Microrobots loaded with x-ray contrast agent were injected through a catheter connected to the rat liver portal vein and steered to the target region under magnetic guidance using a magnetic actuation module (Fig. 7A). For real-time imaging of microrobot in vivo tests, we selected x-ray imaging, which is frequently used for blood vessel visualization in liver embolization. Microrobots were magnetically guided to the targeted vessel using a magnetic field of 40 mT and a gradient magnetic field of 1 T/m. The target region was set to the right median lobe (RML) of the rat liver as the right targeting region and the left median lobe (LML) and left lobe (LL) as the left targeting region. X-ray angiography images before microrobot injection showed blood vessels in the LL, RML, and LML of rat liver (Fig. 7, B to D, fig. S20, and movie S7). After the injection of x-ray contrast agent–loaded microrobots, they were delivered to each targeted vessel within seconds under magnetic guidance using the magnetic actuation module. The delivery of microrobots to each target vessel was confirmed with real-time x-ray imaging. X-ray angiography showed that microrobots blocked all vessels without magnetic guidance (Fig. 7B, fig. S20A, and movie S7), whereas microrobots selectively occluded target blood vessels under magnetic guidance (Fig. 7, C and D; fig. S20, B and C; and movie S7). These results imply that vessel embolization by microrobot can block blood flow, further suggesting that it can reduce the supply of oxygen and nutrients to the tumor. Furthermore, angiography was
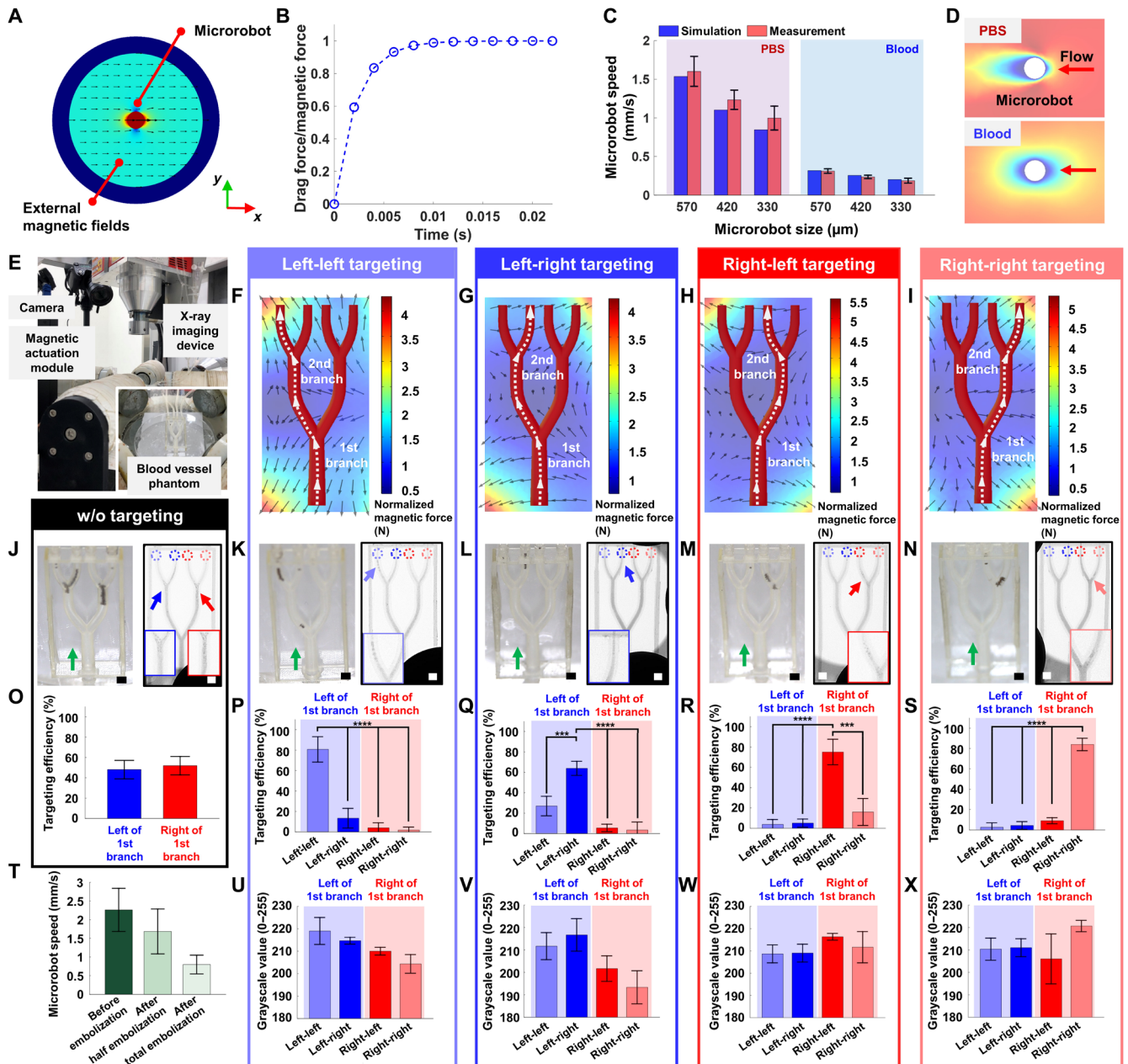
Fig. 6. Evaluation of targeting and real-time x-ray imaging of microrobots and embolization by microrobots using the magnetic actuation module in the vessel phantom. (**A**) Numerical simulation setup for microrobot speed simulation. (**B**) Ratio of drag force and magnetic force acting on the microrobot as a function of time. (**C**) Numerical simulation and measurement of the speed of microrobots of different sizes in different fluids at 40 mT magnetic field and 1 T/m gradient magnetic field ($n = 5$; means ± SD). (**D**) Numerical simulation of fluid behavior around microrobot moving in different fluids. (**E**) Experimental setup for targeting and real-time x-ray imaging of microrobots and embolization using microrobots in the vessel phantom. (**F** to **I**) Numerical simulation of magnetic force map generated using the magnetic actuation module according to target vessel. White dotted arrow line indicates the path of microrobot targeting. (**J** to **N**) Optical and x-ray images after microrobot delivery to target vessel. Green arrow indicates flow direction. Areas near the arrows on x-ray images are presented in the insets. Dotted circles indicate four outlets of the phantom. Scale bars, 5 mm. (**O** to **S**) Microrobot targeting efficiency to target vessel ($n = 5$; means ± SD, ***$P < 0.001$ and ****$P < 0.0001$, Student's t test). (**T**) Microrobot speed according to vessel blocking of phantom ($n = 5$; means ± SD). (**U** to **X**) Grayscale values at four outlets after microrobot targeting followed by injection of iodinated contrast agent. (K to N) The four outlets are indicated by dotted circles on x-ray images ($n = 5$; means ± SD).

performed after recovering RML-embolized rats for 2 weeks (Fig. 7E and movie S7). X-ray angiography indicated that a part of the vessel was opened by microrobot degradation.

We performed MRI of the rat liver as postimaging to verify microrobot targeting. Similar to the results of x-ray imaging, MRI revealed

that microrobots were spread in the entire liver when magnetic guidance was not used, whereas microrobots were mostly located in the target lobe of the liver when magnetic guidance was used (Fig. 7F). We analyzed the microrobot targeting efficiency using MRI (Fig. 7G). The targeting efficiency without magnetic guidance was 43%, with
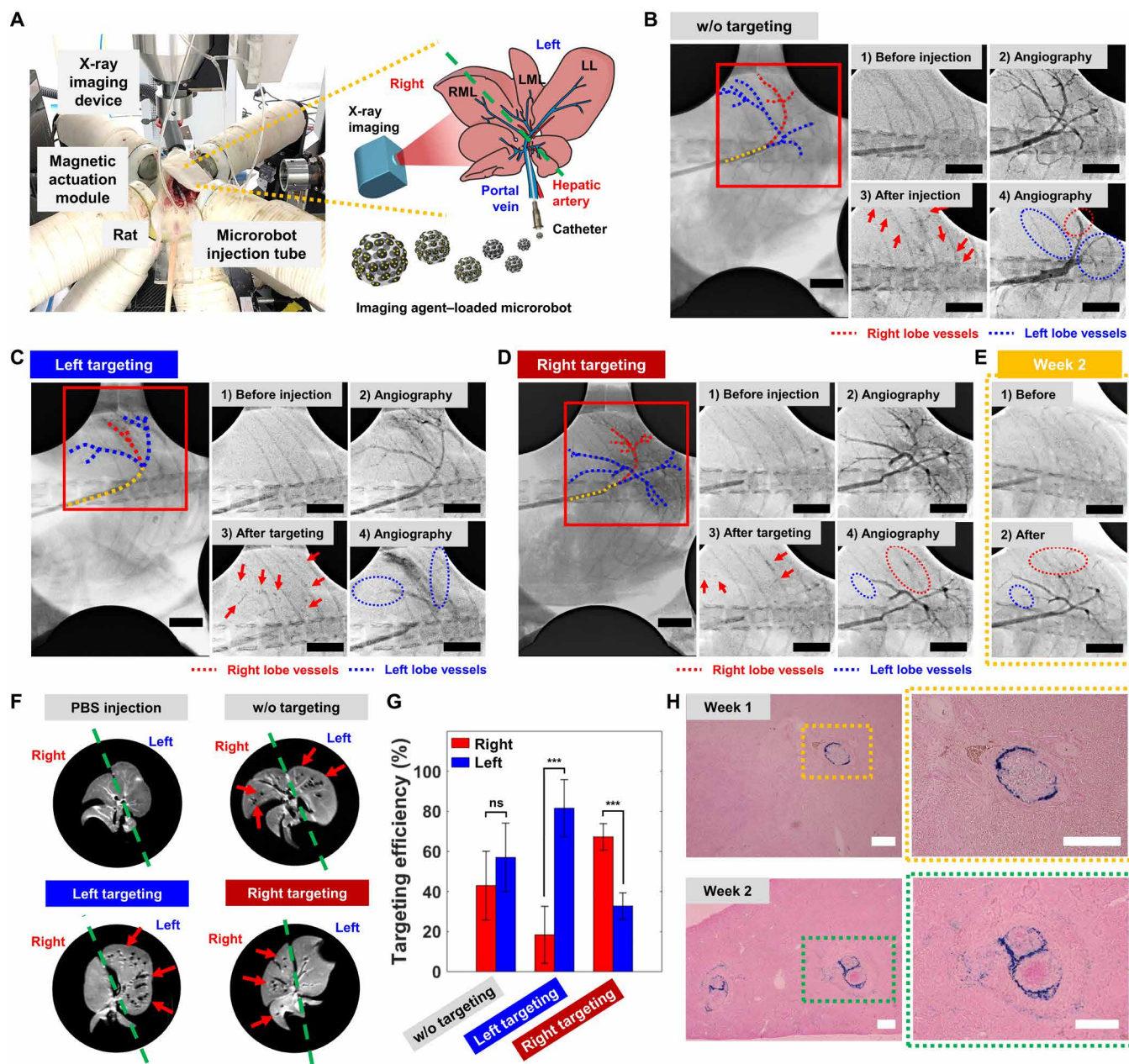
Fig. 7. Evaluation of targeted vessel embolization and degradation of microrobots in vivo. (**A**) Experimental setup and schematic illustration of targeting and real-time x-ray imaging of microrobots and embolization using microrobots in vivo. (**B** to **D**) X-ray angiography images of the portal vein in RML, LL, and LML of the rat liver before and after microrobot delivery. (B) w/o targeting means microrobot delivery without magnetic targeting. The target regions of microrobots are (C) LL and LML, referred to as left targeting, and (D) RML, referred to as right targeting. Red boxes on the left of x-ray images are areas near the arrows that are presented in four insets. Scale bars, 10 mm. (**E**) X-ray angiography images of the portal vein after 2 weeks of right targeting of microrobots. Scale bars, 10 mm. (**F**) MRI of rat livers after PBS injection, w/o targeting, left targeting, and right targeting. Red arrows indicate microrobots delivered to the rat liver. (**G**) Targeting efficiency of microrobots to target vessel ($n = 4$; means ± SD, ***$P < 0.001$, Student's t test). (**H**) Microscopic images of Prussian blue staining at the first week and 2 weeks after microrobot delivery. Scale bars, 500 μm.

almost the same number of microrobots in both the lobes. On the other hand, targeting efficiency to the left and right lobes with magnetic guidance was 81.6 and 67.3%, respectively. The difference in the targeting efficiency of microrobots to the left and right lobes was caused by the magnetic field generation error of the magnetic actuation module and the difference in blood flow velocity to the middle and left lobe branches of the rat portal vein. The left targeting region,

LML and LL, occupies half of the rat liver and requires more blood flow than the right targeting region, RML, which occupies 25% of the rat liver. However, despite the harsh environment, microrobots could overcome blood flow to the LML and LL and be delivered into the RML under magnetic guidance.

To verify the suitability of the microrobot for temporary insertion into the body, microrobot degradation was observed for 2 weeks

after targeting. The shape change and degradation of the microrobot were analyzed by hematoxylin and eosin and Prussian blue iron staining, which revealed the tissue structure and presence of MNPs, respectively (Fig. 7H and fig. S21). The staining image in the first week showed that the microrobots are stacked on a blood vessel and are deformed according to the size and shape of the vessel. The gelatin beads of the microrobot were stably maintained, and MNPs were present on the surface of the microrobot. These results indicate that the gelatin beads were delivered to the target vessel without loss from the microrobot. At week 2, the presence of the microrobot's gelatin beads was not optically confirmed, and MNPs were released from the microrobot and spread in the tissue. The degradation of gelatin in these microrobots is similar to that of commercialized gelatin-based embolic beads (2 to 6 weeks) (*50*). As a result, the microrobot not only can occlude blood vessels according to the size and shape of the blood vessels using a deformable shape but also can be slowly degraded in vivo.

In vivo tumor treatment using the microrobot system

To verify the in vivo tumor treatment of the developed microrobot system, targeted vessel embolization and drug delivery were performed in rats with the orthotopic tumor in LL using the microrobot (Fig. 8A). DOX and iodinated contrast agent were loaded onto 200 microrobots, and an intravascular catheter (20 gauge) was inserted into the portal vein of a rat. A total of 200 DOX-loaded microrobots were injected in bulk at one time through a tube using a syringe pump. After their injection, the microrobots were simultaneously guided to the target region using the magnetic actuation module. Microrobot injection and targeting were completed within tens of seconds (Fig. 8, B and C, and movie S8). The targeted microrobots blocked the target vessel, and DOX released from microrobots was delivered to the tumor.

To determine the tumor treatment efficacy of the microrobot system, rats with orthotopic tumors were assigned to five groups (three rats per group): (i) control (PBS injection), (ii) without microrobot
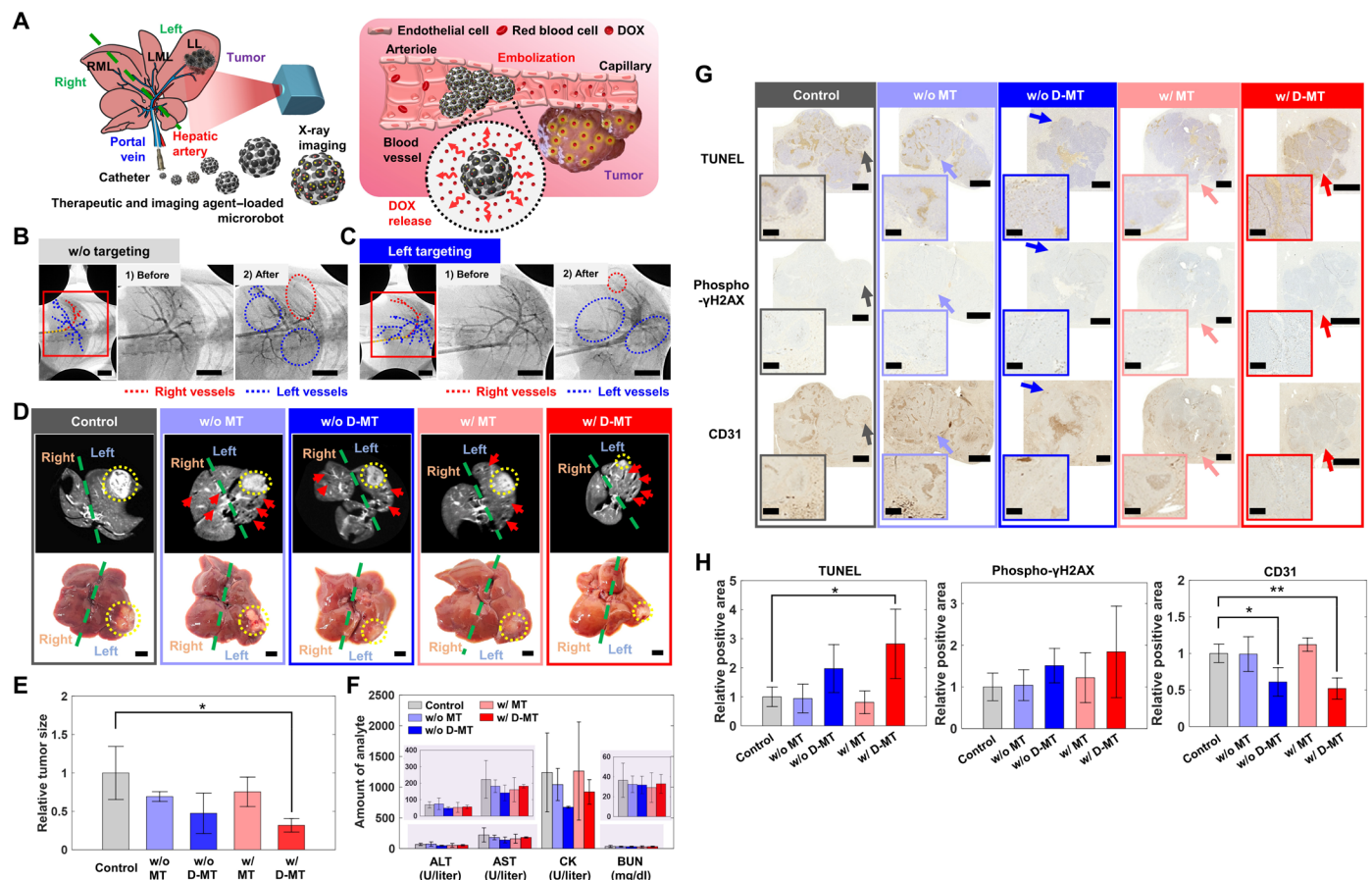

Fig. 8. Evaluation of in vivo tumor treatment using microrobot system. (**A**) Schematic illustration of in vivo tumor treatment using the microrobot system. (**B** and **C**) X-ray angiography images of the portal vein in the RML, LL, and LML of rat liver before and after microrobot delivery. (B) w/o targeting means microrobot delivery without magnetic targeting. The target regions of microrobots are (C) LL and LML, referred to as left targeting. Red boxes on the left of x-ray images are areas near the arrows that are presented in four insets. Scale bars, 10 mm. (**D**) MR and optical images of livers of rats in all five groups. The five groups are the control, without microrobot targeting (w/o MT), without DOX-loaded microrobot targeting (w/o D-MT), with microrobot targeting (w/ MT), and with DOX-loaded microrobot targeting (w/ D-MT) groups. Red arrows on MR images indicate microrobots delivered to the rat liver. Yellow circles indicate liver tumors in rats. Scale bars, 5 mm. (**E**) The size of liver tumors in rats of all five groups ($n = 3$; means ± SD, *$P < 0.05$, Student's t test). (**F**) Blood chemistry results (ALT, AST, CK, and BUN) of all five groups ($n = 3$; means ± SD). (**G**) TUNEL, phospho-γH2AX, and CD31 staining images of rats with liver tumor in all five groups. Scale bars, 2 mm. The areas near the arrows are presented in the insets. Scale bars (insets), 1 mm. (**H**) Relative TUNEL-, phospho-γH2AX–, and CD31-positive areas in tumor sections of the rat liver for all five groups ($n = 3$; means ± SD, *$P < 0.05$ and **$P < 0.01$, Student's t test).

targeting (w/o MT), (iii) without DOX-loaded microrobot targeting (w/o D-MT), (iv) with microrobot targeting (w/ MT), and (v) with DOX-loaded microrobot targeting (w/ D-MT). The right and left target vessels of rats in the microrobot-injected groups were visualized before microrobot injection on x-ray angiography using the x-ray contrast agent (Fig. 8, B and C, before, and movie S8). All vessels appeared blocked on x-ray angiography after microrobot injection in the group without targeting (Fig. 8B, after, and movie S8). On the other hand, in the group with targeting using the magnetic actuation module, most of the microrobots were delivered to the left vessel where the orthotopic tumor was located, and the x-ray contrast agent could not pass through this vessel because of the embolic effect of the microrobots (Fig. 8C, after, and movie S8). In all groups, the rats survived the injection of N1S1 cells and the surgery procedure. In particular, rats in the w/ D-MT group survived the injection of x-ray contrast agents and the injection and targeting of drug-loaded microrobots.

After 10 days of the microrobot treatment, we euthanized the rats of all five groups and investigated the microrobot position and liver tumor size by MRI and visual observation (Fig. 8, D and E). MRI of the w/o MT and w/o D-MT groups showed that microrobots were present in the entire liver. On the other hand, MRI of the w/ MT and w/ D-MT groups revealed that most microrobots were located in LL with tumor. The MRI and gross observation revealed that the tumor size tended to decrease on average in the microrobot-injected groups without DOX compared with the control group (w/o MT and w/ MT), but without significant difference. On the other hand, the tumor size was substantially reduced on average in the groups injected with DOX-loaded microrobots (w/o D-MT and w/ D-MT) compared with the control group. In particular, significant tumor size reduction was observed in the microrobot targeting group (w/ D-MT). Hence, we believe that targeted vessel embolization and drug delivery using the microrobot system may have a synergistic effect that provides a long-lasting drug effect with a decrease in blood flow.

To confirm the microrobot biocompatibility in vivo, blood chemical analysis was performed using markers related to liver, heart, and kidney damage (Fig. 8F). We measured alanine aminotransferase (ALT) and aspartate aminotransferase (AST) for hepatic function, creatine kinase (CK) for cardiac function, and blood urea nitrogen (BUN) for kidney function on day 10 after treatment (62). The microrobot treatment did not increase the mean values of all the four parameters—namely, ALT, AST, CK, and BUN—in all experimental animals. The mean values of ALT, AST, CK, and BUN in all experimental groups were 60.06 ± 11.03 U/liter, 177.66 ± 30.44 U/liter, 1028.6 ± 243.28, and 32.62 ± 2.63 mg/dl, respectively. According to the Lab Anim Res (63), the mean ALT values in 13-week-old male and female Sprague-Dawley rats were 31.2 ± 5.8 and 29.9 ± 10.3 U/liter (range: 18 to 45 U/liter), respectively, and the mean AST values in 13-week-old male and female Sprague-Dawley rats were 85.8 ± 18.5 and 82.8 ± 23.2 U/liter (range: 74 to 143 U/liter), respectively. In addition, the CK and BUN values in the animals exposed to the microrobot treatment were in the normal range, indicating biosafety. Furthermore, the weights of the liver, spleen, and kidney were measured to investigate organ damage (fig. S22). The average liver weight was low in the DOX-loaded microrobot without targeting group, but without significance, because DOX had spread throughout the liver. The weight of organs between the remaining groups showed no significance. Hence, we confirmed the in vivo biocompatibility of the

proposed microrobot system and that the toxicity caused by intravascular administration of the drug can be improved by delivering the drug locally.

To investigate the tumor treatment effect of the microrobot system, we performed histological analysis of tumor-bearing liver tissue, terminal deoxynucleotidyl transferase–mediated deoxyuridine triphosphate nick end labeling (TUNEL) assay, and immunohistochemical staining for phosphorylated histone H2AX (phospho-γH2AX) and CD31 (Fig. 8, G and H, and fig. S23). TUNEL, phospho-γH2AX, and CD31 staining assays were performed to evaluate tumor apoptosis, DNA damage caused by DOX, and angiogenesis around the tumor, respectively. The results revealed higher tumor cell apoptosis and DNA damage and lower peritumoral angiogenesis in groups treated with drug-loaded microrobots (w/ D-MT and w/o D-MT) than in the control and microrobot without drug loading (w/o MT and w/ MT) groups. In addition, we obtained the relative positive areas of TUNEL, phospho-γH2AX, and CD31 compared to the tumor area by postprocessing the staining images (fig. S24). Except for phospho-γH2AX staining, drug-loaded microrobot using magnetic targeting in TUNEL and CD31 staining exhibited significance compared to the control (Fig. 8H). Although we did not see the tumor treatment effect of microrobot target vessel embolization alone without drug, targeting of drug-loaded microrobot revealed a positive effect on tumor treatment in terms of tumor size and histological analysis results.

DISCUSSION
We developed a real-time MRI-guided microrobot system for liver chemoembolization. First, we developed microrobots of several sizes (300 to 600 μm) for use in blood vessels of different morphologies, similar to clinically approved embolic beads. MNPs on the microrobot surface enabled magnetic actuation and observation on MRI. In addition, the elastic properties of microrobots provided high adaptability to be injected through the microcatheter and help to occlude the vessel effectively. Furthermore, imaging and therapeutic agents could be loaded into microrobots, enabling real-time imaging (ultrasound and x-ray) and treatment of tumors through drug (DOX and 5-FU) delivery. Furthermore, a magnetic actuation module was introduced to deliver the microrobot to the target vessel. The magnetic actuation module, composed of nine electromagnetic coils, was fabricated by optimizing the coil placement considering the animal, x-ray imaging device, microrobot injection device, and microrobot locomotion in 3D space. The developed magnetic actuation module could deliver microrobots to the target vessel through two branches in the phantom by generating a high-intensity magnetic field at two points in the workspace. As a practical biomedical application, in vivo validation of the microrobot system was performed through targeted vessel embolization and drug delivery in a rat model of orthotopic liver tumor. Microrobots injected into the portal vein under magnetic guidance using x-ray imaging occluded the target vessel and treated the tumor by releasing the drug. Although the developed microrobot system has targeting and drug delivery properties in vivo, several major challenges should be addressed before clinical trials can be conducted.

Biocompatibility and biodegradability of microrobots are essential to prevent the potential toxicity of microrobot components and adverse effects caused by untargeted microrobots. In this study, we investigated the in vivo biocompatibility and biodegradation of

microrobots for 2 weeks. The results revealed that microrobots did not cause damage to organs and that MNPs spread into the liver tissue as the microrobots slowly degraded. However, in vivo mid- and long-term implantation of microrobots is required to determine the actual rate of degradation and local toxic effects of all degradable substances (*64*, *65*). Therefore, we will analyze the period required for complete degradation of microrobots in vivo and the long-term effects on the organs and blood. The x-ray imaging agent (OMNIPAQUE 300) loaded on the microrobot has been clinically approved, is rapidly released from the microrobot, and can be quickly removed by the kidneys. In the in vivo experiment, we confirmed that there was no difference in BUN for kidney function (Fig. 8F) and kidney weight (fig. S22C) between the control and microrobot injection groups. However, when large amounts of microrobots are injected into the body, renal damage may occur due to the hyperosmolality induced by the high viscosity and high iodine concentrations (*66*). Therefore, to overcome the shortcoming, we will test biocompatibility and real-time imaging duration by experimenting with several imaging agent candidates, including gold nanoparticles in microrobots.

Although we confirmed that the gelatin beads of the microrobot are delivered to the target vessel without loss and are slowly degraded, the nontargeted microrobot or gelatin released from the microrobot may cause vessel embolization to other organs or the formation of blood clots. We will continue to conduct animal experiments to confirm the induction of these side effects. To avoid these side effects, we plan to study methods to recover nontargeted microrobots and materials or selectively remove them by applying external stimuli. In addition, instead of gelatin, which promotes thrombus formation, we will design and fabricate microrobots made of natural or synthetic polymers with biocompatibility and biodegradability.

The magnetic actuation module was optimally designed to deliver the microrobots to the tumor feeding vessel and avoid interference with animals (i.e., the patient), x-ray imaging, and microrobot injection devices. The magnetic actuation module can generate a maximum magnetic field of 70 mT and a maximum gradient magnetic field of 1.7 T/m. Also, the focused magnetic fields formed at two points could magnetically guide the microrobots to the target vessel through the two branches successively without additional control during microrobot targeting. However, for clinical application, the magnetic actuation module should be developed to fit the target organ in humans by increasing the scale. In particular, the magnetic field intensity generated from the coil rapidly decreases with distance. Therefore, in the scale-up stage, the magnetic actuation module needs to generate sufficient magnetic field intensity to magnetize the microrobot. In addition, compared with the proposed magnetic actuation module for rats, the large-sized module for humans may cause lag time according to the direction change of the magnetic field during the microrobot targeting. To solve these problems, we will develop a magnetic actuation module that generates strong magnetic field intensities and, at the same time, is compatible with humans, x-ray imaging, and microrobot injection devices. Furthermore, using the visualized blood vessel obtained through x-ray imaging, we will form the focused magnetic fields to guide the microrobot to the targeted region at once without changing the direction of the magnetic fields. In addition, because the liver blood arteries in humans have more branches (*29*), the magnetic actuation module necessitates microrobot targeting of more than three branches along with microcatheter superselection. Therefore, we will develop a magnetic actuation module capable of microrobot superselection

for multiple branches. Next, although the balloon catheter occludes the blood vessel, weak blood flow is still present. In addition, the rapid blood flow into the narrow gap between the catheter and the blood vessel may make it more difficult to steer the microrobots in the closer bifurcations. We will design the magnetic actuation module for humans to generate stronger magnetic fields than those developed now so that microrobots can be guided to the targeted vessel even at high blood flow.

In terms of microrobot powering mechanism, since microrobot actuation using gradient magnetic fields requires high magnetic field strength, it needs high power and a large volume of magnetic actuation module compared to other actuation methods such as light, ultrasound, and chemical reaction. To overcome these limitations, we are developing a next-generation magnetic actuation module that can increase the driving performance of microrobots and have low power consumption and a small volume. Along with magnetic field–based microrobot manipulation, we are studying an ultrasonic actuation module capable of 3D locomotion of microrobots in deep tissue (*67*). As a prototype type of ultrasonic actuation module, we have confirmed that the microrobot can move in three dimensions within a phantom, including porcine tissue. In future work, we will develop magnetic and ultrasonic-based microrobot actuation modules that can accommodate the human body.

In the in vivo validation of tumor treatment using the microrobot system, we did not find any significant therapeutic effect by vessel embolization when microrobots were targeted without drugs, despite target vessel embolization using microrobots. There are two reasons for this result. First, vessel embolization using embolic beads is performed clinically in the hepatic artery, which is the main nutrient supplier for tumors. However, in this study, we could not use microrobots with a diameter used in clinical tests (300 to 600 μm) in a small-sized hepatic artery of the rat liver (approximately 250 μm) (*68*). Therefore, the in vivo experiment using the microrobot system was performed by injecting microrobots into a relatively large portal vein (approximately 2 mm) (*68*). Next, vascular occlusion by embolic beads can cause ischemic tumor necrosis by blocking the supply of nutrients to the tumor feeding vessel. However, vessel embolization using only microrobot without drugs cannot effectively treat the tumor. Therefore, in most clinical cases, embolic beads and drugs are administered simultaneously (*27*, *41*). This chemoembolization reduces the blood flow in the tumor tissue, and the injected drugs stay in the tumor tissue at a high concentration for a long time. Because of ischemia, the pump function of the tumor cell membrane is lowered, and many drugs enter tumor cells, thereby exhibiting a higher anticancer effect. Although we did not observe any antitumor effect of targeted vessel embolization using microrobots, a significant reduction in the tumor was observed after DOX release from the microrobot in the target vessel. These results reveal that we expect blood flow to decrease with blood vessel occlusion by the microrobot and that DOX will be present longer in liver tissues and enhance the anticancer effect. Moreover, the N1S1 cell–based rat liver tumor model used in this study allowed a complex catheter insertion technique that is used clinically in interventional radiology and has the advantage of imaging by conventional radiological methods (*69*). However, in the liver tumor rat model, self-regression of the tumor is known to occur after 2 weeks (*69*). Therefore, another limitation of our study is that validation of in vivo tumor treatment with the microrobot system was limited to 10 days. In the future, we intend to compensate for the drawbacks by performing mid- to

long-term in vivo validation tests of the microrobot system in a medium-sized animal model of the tumor in which microrobots can be injected into the hepatic artery.

MATERIALS AND METHODS

Detailed fabrication and characterization of the microrobot are explained in sections S1 to S4 of the Supplementary Materials. In addition, detailed protocols of in vitro, phantom, and in vivo tests are presented in sections S10 to S16 of the Supplementary Materials.

Experimental setup for microrobot targeting using the magnetic actuation module

Nine electromagnetic coils and pure iron cores of the electromagnetic actuation (EMA) system were obtained from JL Magnet (South Korea). An optical microscope (F170, Carl Zeiss, Germany), digital single-lens reflex camera (DSLR) camera (EOS 600D, CANON, Japan), and x-ray imaging device were easily accessible in the workspace without interference of the EMA system and useful for observing the movement of microrobots. The EMA system was controlled using the LabVIEW software (National Instruments, Austin, Texas, USA), and nine power supplies (each set of MX 15 and 3001 ix, AMETEK, USA) were used to apply current in nine coils.

To test targeting, real-time x-ray imaging, and embolization using microrobots in the vessel phantom, the phantom was designed considering the smallest branch of the human hepatic artery accessible to the microcatheter. In detail, considering that the catheter cannot access vessels less than twice the diameter of a catheter (27), only a 1.4-Fr microcatheter (outer diameter: 0.57 mm) can access the six branches (diameter: about 1.3 mm) of the human hepatic artery (29). On the basis of the clinically limited access of the catheter, two branches of the phantom corresponding to the seven (diameter: about 0.7 mm) and eight branches (diameter: about 0.96 mm) of the human hepatic artery were designed and fabricated using a 3D printer (Objet30 Pro, Stratasys, USA) (fig. S16). Microrobots with iodinated contrast agent were guided magnetically using a magnetic actuation module in real time with x-ray irradiation (100 kV, 100 μA) in the vessel phantom. During targeting, microrobots were flowed at a rate of 2 ml/min (= fluid injection speed of ~2.5 cm/s). Here, the flow rate was determined by considering the diameter (~1.3 mm) of the six branches (29) and the number of blood vessels (~166) (29) based on the diameter (~4.1 mm) (70) and blood velocity (~45 cm/s) (70) of the main vessel of the human hepatic artery. After microrobot targeting, an iodinated contrast agent was injected into the phantom to confirm flow block by target vessel embolization. The flow block of the channel in the phantom was confirmed on the basis of the change in x-ray contrast agent observed in the four outlets on the recorded image. To confirm this quantitatively, the grayscale values of four outlets in each frame of the video were measured using ImageJ software (National Institutes of Health, USA). The flow blocking of the channel in the phantom was observed on the recorded image as the change in the amount of x-ray contrast agent in the four outlets. To confirm this quantitatively, the grayscale values of four outlets in each frame of the video were measured using ImageJ software (National Institutes of Health, USA).

Statistics and data analysis

All experimental data were compared using Student's t test. All data are presented as means ± SD. The differences between groups were considered statistically significant at *$P < 0.05$ and highly significant at **$P < 0.01$, ***$P < 0.001$, and ****$P < 0.0001$.

SUPPLEMENTARY MATERIALS

Supplementary material for this article is available at https://science.org/doi/10.1126/sciadv.abq8545

REFERENCES AND NOTES

1. M. Sitti, H. Ceylan, W. Hu, J. Giltinan, M. Turan, S. Yim, E. Diller, Biomedical applications of untethered mobile milli/microrobots. *Proc. IEEE* **103**, 205–224 (2015).
2. H. Ceylan, J. Giltinan, K. Kozielski, M. Sitti, Mobile microrobots for bioengineering applications. *Lab Chip* **17**, 1705–1724 (2017).
3. S. Palagi, P. Fischer, Bioinspired microrobots. *Nat. Rev. Mater.* **3**, 113–124 (2018).
4. M. Koleoso, X. Feng, Y. Xue, Q. Li, T. Munshi, X. Chen, Micro/nanoscale magnetic robots for biomedical applications. *Mater. Today Bio.* **8**, 100085 (2020).
5. F. Soto, E. Karshalev, F. Zhang, B. E. F. de Avila, A. Nourhani, J. Wang, Smart materials for microrobots. *Chem. Rev.* **122**, 5365–5403 (2021).
6. Z. Li, C. Li, L. Dong, J. Zhao, A review of microrobot's system: Towards system integration for autonomous actuation in vivo. *Micromachines* **12**, 1249 (2021).
7. B. Wang, Y. Zhang, L. Zhang, Recent progress on micro- and nano-robots: Towards in vivo tracking and localization. *Quant. Imaging Med. Surg.* **8**, 461–479 (2018).
8. X. Yan, Q. Zhou, M. Vincent, Y. Deng, J. Yu, J. Xu, T. Xu, T. Tang, L. Bian, Y.-X. J. Wang, K. Kostarelos, L. Zhang, Multifunctional biohybrid magnetite microrobots for imaging-guided therapy. *Sci. Robot.* **2**, eaaq1155 (2017).
9. A. Servant, F. Qiu, M. Mazza, K. Kostarelos, B. J. Nelson, Controlled in vivo swimming of a swarm of bacteria-like microrobotic flagella. *Adv. Mater.* **27**, 2981–2988 (2015).
10. J. Li, X. Li, T. Luo, R. Wang, C. Liu, S. Chen, D. Li, J. Yue, S.-H. Cheng, D. Sun, Development of a magnetic microrobot for carrying and delivering targeted cells. *Sci. Robot.* **3**, eaat8829 (2018).
11. S. Jeon, S. Kim, S. Ha, S. Lee, E. Kim, S. Y. Kim, S. H. Park, J. H. Jeon, S. W. Kim, C. Moon, B. J. Nelson, J.-Y. Kim, S.-W. Yu, H. Choi, Magnetically actuated microrobots as a platform for stem cell transplantation. *Sci. Robot.* **4**, eaav4317 (2019).
12. D. Li, C. Liu, Y. Yang, L. Wang, Y. Shen, Micro-rocket robot with all-optic actuating and tracking in blood. *Light Sci. Appl.* **9**, 84 (2020).
13. T. Wei, J. Liu, D. Li, S. Chen, Y. Zhang, J. Li, L. Fan, Z. Guan, C.-M. Lo, L. Wang, K. Man, D. Sun, Development of magnet-driven and image-guided degradable microrobots for the precise delivery of engineered stem cells for cancer therapy. *Small* **16**, 1906908 (2020).
14. Z. Jin, K. T. Nguyen, G. Go, B. Kang, H.-K. Min, S.-J. Kim, Y. Kim, H. Li, C.-S. Kim, S. Lee, S. Park, K.-P. Kim, K. M. Huh, J. Song, J.-O. Park, E. Choi, Multifunctional nanorobot system for active therapeutic delivery and synergistic chemo-photothermal therapy. *Nano Lett.* **19**, 8550–8564 (2019).
15. P. Pouponneau, J.-C. Leroux, G. Soulez, S. Martel, Co-encapsulation of magnetic nanoparticles and doxorubicin into biodegradable microcarriers for deep tissue targeting by vascular MRI navigation. *Biomaterials* **32**, 3481–3486 (2011).
16. H. Zhang, Z. Li, C. Gao, X. Fan, Y. Pang, T. Li, Z. Wu, H. Xie, Q. He, Dual-responsive biohybrid neutrobots for active target delivery. *Sci. Robot.* **6**, eaaz9519 (2021).
17. Z. Wu, L. Li, Y. Yang, P. Hu, Y. Li, S.-Y. Yang, V. Wang Lihong, W. Gao, A microrobotic system guided by photoacoustic computed tomography for targeted navigation in intestines in vivo. *Sci. Robot.* **4**, eaax0613 (2019).
18. G. Go, S.-G. Jeong, A. Yoo, J. Han, B. Kang, S. Kim, T. Nguyen Kim, Z. Jin, C.-S. Kim, R. Seo Yu, Y. Kang Ju, Y. Na Ju, K. Song Eun, Y. Jeong, K. Seon Jong, J.-O. Park, E. Choi, Human adipose–derived mesenchymal stem cell–based medical microrobot system for knee cartilage regeneration in vivo. *Sci. Robot.* **5**, eaay6626 (2020).
19. B. Wang, K. F. Chan, K. Yuan, Q. Wang, X. Xia, L. Yang, H. Ko, Y.-X. J. Wang, J. J. Y. Sung, P. W. Y. Chiu, L. Zhang, Endoscopy-assisted magnetic navigation of biohybrid soft microrobots with rapid endoluminal delivery and imaging. *Sci. Robot.* **6**, eabd2813 (2021).
20. A. Aziz, S. Pane, V. Iacovacci, N. Koukourakis, J. Czarske, A. Menciassi, M. Medina-Sánchez, O. G. Schmidt, Medical imaging of microrobots: Toward in vivo applications. *ACS Nano* **14**, 10865–10893 (2020).
21. S. Pané, J. Puigmartí-Luis, C. Bergeles, X.-Z. Chen, E. Pellicer, J. Sort, V. Počepcová, A. Ferreira, B. J. Nelson, Imaging technologies for biomedical micro- and nanoswimmers. *Adv. Mater. Technol.* **4**, 1800575 (2019).
22. J. Yu, D. Jin, K.-F. Chan, Q. Wang, K. Yuan, L. Zhang, Active generation and magnetic actuation of microrobotic swarms in bio-fluids. *Nat. Commun.* **10**, 5631 (2019).
23. Q. Wang, K. F. Chan, K. Schweizer, X. Du, D. Jin, S. C. H. Yu, B. J. Nelson, L. Zhang, Ultrasound Doppler-guided real-time navigation of a magnetic microswarm for active endovascular delivery. *Sci. Adv.* **7**, eabe5914 (2021).
24. L. Li, L. Zhu, C. Ma, L. Lin, J. Yao, L. Wang, K. Maslov, R. Zhang, W. Chen, J. Shi, L. V. Wang, Single-impulse panoramic photoacoustic computed tomography of small-animal

whole-body dynamics at high spatiotemporal resolution. *Nat. Biomed. Eng.* **1**, 0071 (2017).

25. F. Michaud, N. Li, R. Plantefève, Z. Nosrati, C. Tremblay, K. Saatchi, G. Moran, A. Bigot, U. O. Häfeli, S. Kadoury, A. Tang, P. Perreault, S. Martel, G. Soulez, Selective embolization with magnetized microbeads using magnetic resonance navigation in a controlled-flow liver model. *Med. Phys.* **46**, 789–799 (2019).

26. Z. Nosrati N. Li, F. Michaud, S. Ranamukhaarachchi, S. Karagiozov, G. Soulez, S. Martel, K. Saatchi, U. O. Häfeli, Development of a coflowing device for the size-controlled preparation of magnetic-polymeric microspheres as embolization agents in magnetic resonance navigation technology. *ACS Biomater. Sci. Eng.* **4**, 1092–1102 (2018).

27. Y.-X. J. Wáng, T. De Baere, J.-M. Idée, S. Ballet, Transcatheter embolization therapy in liver cancer: An update of clinical evidences. *Chin. J. Cancer Res.* **27**, 96–121 (2015).

28. M. Caine, D. Carugo, X. Zhang, M. Hill, M. R. Dreher, A. L. Lewis, Review of the development of methods for characterization of microspheres for use in embolotherapy: Translating bench to cathlab. *Adv. Healthc. Mater.* **6**, 1601291 (2017).

29. C. Debbaut, P. Segers, P. Cornillie, C. Casteleyn, M. Dierick, W. Laleman, D. Monbaliu, Analyzing the human liver vascular architecture by combining vascular corrosion casting and micro-CT scanning: A feasibility study. *J. Anat.* **224**, 509–517 (2014).

30. A. Pérez-López, C. Martín-Sabroso, L. Gómez-Lázaro, A. I. Torres-Suárez, J. Aparicio-Blanco, Embolization therapy with microspheres for the treatment of liver cancer: State-of-the-art of clinical translation. *Acta Biomater.* **149**, 1–15 (2022).

31. Y. P. Chen, J. L. Zhang, Y. Zou, Y. L. Wu, Recent advances on polymeric beads or hydrogels as embolization agents for improved transcatheter arterial chemoembolization (TACE). *Front. Chem.* **7**, 408 (2019).

32. D.-H. Kim, W. Li, J. Chen, Z. Zhang, R. M. Green, S. Huang, A. C. Larson, Multimodal imaging of nanocomposite microspheres for transcatheter intra-arterial drug delivery to liver tumors. *Sci. Rep.* **6**, 29653 (2016).

33. H. Choi, B. Choi, B. Yu, W. Li, M. M. Matsumoto, K. R. Harris, R. J. Lewandowski, A. C. Larson, S. K. Mouli, D.-H. Kim, On-demand degradable embolic microspheres for immediate restoration of blood flow during image-guided embolization procedures. *Biomaterials* **265**, 120408 (2021).

34. H. Albadawi, I. Altun, J. Hu, Z. Zhang, A. Panda, H.-J. Kim, A. Khademhosseini, R. Oklu, Nanocomposite hydrogel with tantalum microparticles for rapid endovascular hemostasis. *Adv. Sci.* **8**, 2003327 (2021).

35. J. Hu, H. Albadawi, Z. Zhang, M. A. Salomao, S. Gunduz, S. Rehman, L. D'Amone, J. L. Mayer, F. Omenetto, R. Oklu, Silk embolic material for catheter-directed endovascular drug delivery. *Adv. Mater.* **34**, 2106865 (2022).

36. L.-S. Lin, Z.-X. Cong, J.-B. Cao, K.-M. Ke, Q.-L. Peng, J. Gao, H.-H. Yang, G. Liu, X. Chen, Multifunctional Fe$_3$O$_4$@polydopamine core–shell nanocomposites for intracellular mrna detection and imaging-guided photothermal therapy. *ACS Nano* **8**, 3876–3883 (2014).

37. P. Mishra, B. Nayak, R. K. Dey, PEGylation in anti-cancer therapy: An overview. *Asian J. Pharm.* **11**, 337–348 (2016).

38. J. H. Maeng, D.-H. Lee, K. H. Jung, Y.-H. Bae, I.-S. Park, S. Jeong, Y.-S. Jeon, C.-K. Shim, W. Kim, J. Kim, J. Lee, Y.-M. Lee, J.-H. Kim, W.-H. Kim, S.-S. Hong, Multifunctional doxorubicin loaded superparamagnetic iron oxide nanoparticles for chemotherapy and magnetic resonance imaging in liver cancer. *Biomaterials* **31**, 4995–5006 (2010).

39. N. Singh, G. J. S. Jenkins, R. Asadi, S. H. Doak, Potential toxicity of superparamagnetic iron oxide nanoparticles (SPION). *Nano Rev.* **1**, 5358 (2010).

40. M. Mahmoudi, S. Sant, B. Wang, S. Laurent, T. Sen, Superparamagnetic iron oxide nanoparticles (SPIONs): Development, surface modification and applications in chemotherapy. *Adv. Drug Deliv. Rev.* **63**, 24–46 (2011).

41. K. Osuga, N. Maeda, H. Higashihara, S. Hori, T. Nakazawa, K. Tanaka, M. Nakamura, K. Kishimoto, Y. Ono, N. Tomiyama, Current status of embolic agents for liver tumor embolization. *Int. J. Clin. Oncol.* **17**, 306–315 (2012).

42. K. Kopeć, M. Wojasiński, M. Eichler, H. Genç, R. P. Friedrich, R. Stein, R. Singh, C. Alexiou, H. Hlawaty, T. Ciach, I. Cicha, Polydopamine and gelatin coating for rapid endothelialization of vascular scaffolds. *Mater. Sci. Eng. C* **134**, 112544 (2021).

43. G. R. Barbeau, Radial loop and extreme vessel tortuosity in the transradial approach: Advantage of hydrophilic-coated guidewires and catheters. *Catheter. Cardiovasc. Interv.* **59**, 442–450 (2003).

44. M. Kinnunen, A. Kauppila, A. Karmenyan, R. Myllylä, Effect of the size and shape of a red blood cell on elastic light scattering properties at the single-cell level. *Biomed. Opt. Express* **2**, 1803–1814 (2011).

45. Z. Kan, D. C. Madoff, Liver anatomy: Microcirculation of the liver. *Semin. Intervent. Radiol.* **25**, 77–85 (2008).

46. C. Janko, J. Zaloga, M. Pöttler, S. Dürr, D. Eberbeck, R. Tietze, S. Lyer, C. Alexiou, Strategies to optimize the biocompatibility of iron oxide nanoparticles—"SPIONs safe by design". *J. Magn. Magn. Mater.* **431**, 281–284 (2017).

47. E. Vey, C. Rodger, J. Booth, M. Claybourn, A. F. Miller, A. Saiani, Degradation kinetics of poly(lactic-co-glycolic) acid block copolymer cast films in phosphate buffer solution as revealed by infrared and Raman spectroscopies. *Polym. Degrad. Stab.* **96**, 1882–1889 (2011).

48. S. Suvarnapathaki, M. A. Nguyen, X. Wu, S. P. Nukavarapu, G. Camci-Unal, Synthesis and characterization of photocrosslinkable hydrogels from bovine skin gelatin. *RSC Adv.* **9**, 13016–13025 (2019).

49. J. Calvarro, T. Perez-Palacios, J. Ruiz, Modification of gelatin functionality for culinary applications by using transglutaminase. *Int. J. Gastron. Food Sci.* **5**, 27–32 (2016).

50. H. Kawano, S. Arakawa, O. Satoh, Y. Matsumoto, M. Hayano, S. Miyabara, Foreign body granulomatous change from absorbable gelatin sponge and microcoil embolization after a guidewire-induced perforation in the distal coronary artery. *Intern. Med.* **49**, 1871–1874 (2010).

51. Y. Minami, M. Kudo, Contrast-enhanced ultrasonography with Sonazoid in hepatocellular carcinoma diagnosis. *Hepatoma Res.* **6**, 46 (2020).

52. J. Estelrich, M. J. Sánchez-Martín, M. A. Busquets, Nanoparticles in magnetic resonance imaging: From simple to dual contrast agents. *Int. J. Nanomedicine* **10**, 1727–1741 (2015).

53. Y. Huang, J. C. Hsu, H. Koo, D. P. Cormode, Repurposing ferumoxytol: Diagnostic and therapeutic applications of an FDA-approved nanoparticle. *Theranostics* **12**, 796–816 (2022).

54. Y. D. Xiao, R. Paudel, J. Liu, C. Ma, Z. S. Zhang, S. K. Zhou, MRI contrast agents: Classification and application (Review). *Int. J. Mol. Med.* **38**, 1319–1326 (2016).

55. Y. Shen, F. L. Goerner, C. Snyder, J. N. Morelli, D. Hao, D. Hu, X. Li, V. M. Runge, T1 relaxivities of gadolinium-based magnetic resonance contrast agents in human whole blood at 1.5, 3, and 7 T. *Invest. Radiol.* **50**, 330–338 (2015).

56. M. N. Moore, Do nanoparticles present ecotoxicological risks for the health of the aquatic environment? *Environ. Int.* **32**, 967–976 (2006).

57. Y.-B. Hu, E. B. Dammer, R.-J. Ren, G. Wang, The endosomal-lysosomal system: From acidification and cargo sorting to neurodegeneration. *Transl. Neurodegener.* **4**, 18 (2015).

58. B. Lin, H. Chen, D. Liang, W. Lin, X. Qi, H. Liu, X. Deng, Acidic pH and high-H$_2$O$_2$ dual tumor microenvironment-responsive nanocatalytic graphene oxide for cancer selective therapy and recognition. *ACS Appl. Mater. Interfaces* **11**, 11157–11166 (2019).

59. P. Swietach, A. Hulikova, S. Patiar, R. D. Vaughan-Jones, A. L. Harris, Importance of intracellular pH in determining the uptake and efficacy of the weakly basic chemotherapeutic drug, doxorubicin. *PLOS ONE* **7**, e35949 (2012).

60. J. Wielińska, A. Nowacki, B. Liberek, 5-Fluorouracil—Complete insight into its neutral and ionised forms. *Molecules* **24**, 3683 (2019).

61. Y. Liu, K. Ai, J. Liu, Y. Deng, Y. He, L. Lu, Dopamine-melanin colloidal nanospheres: An efficient near-infrared photothermal therapeutic agent for in vivo cancer therapy. *Adv. Mater.* **25**, 1353–1359 (2013).

62. L. P. Ganipineni, B. Ucakar, N. Joudiou, J. Bianco, P. Danhier, M. Zhao, C. Bastiancich, B. Gallez, F. Danhier, V. Préat, Magnetic targeting of paclitaxel-loaded poly(lactic-*co*–glycolic acid)-based nanoparticles for the treatment of glioblastoma. *Int. J. Nanomedicine* **13**, 4509–4521 (2018).

63. J.-M. Lee, M.-A. Lee, H.-N. Do, Y.-I. Song, H.-Y. Lee, S. H. Park, J. S. Kang, J.-k. Kang, Historical control data from 13-week repeated toxicity studies in Crj: CD (SD) rats. *Lab. Anim. Res.* **28**, 115–121 (2012).

64. L. Weng, M. Rusten, R. Talaie, M. Hairani, N. K. Rosener, J. Golzarian, Calibrated bioresorbable microspheres: A preliminary study on the level of occlusion and arterial distribution in a rabbit kidney model. *J. Vasc. Interv. Radiol.* **24**, 1567–1575 (2013).

65. R. J. Owen, P. N. Nation, R. Polakowski, J. A. Biliske, P. B. Tiege, I. J. Griffith, A preclinical study of the safety and efficacy of occlusin™ 500 artificial embolization device in sheep. *Cardiovasc. Intervent. Radiol.* **35**, 636–644 (2012).

66. H. Lusic, M. W. Grinstaff, X-ray-computed tomography contrast agents. *Chem. Rev.* **113**, 1641–1666 (2013).

67. H. X. Cao, D. Jung, H.-S. Lee, G. Go, M. Nan, E. Choi, C.-S. Kim, J.-O. Park, B. Kang, Micromotor manipulation using ultrasonic active traveling waves. *Micromachines* **12**, 192 (2021).

68. P. N. A. Martins, P. Neuhaus, Surgical anatomy of the liver, hepatic vasculature and bile ducts in the rat. *Liver Int.* **27**, 384–392 (2007).

69. M. Buijs, J.-F. H. Geschwind, L. H. Syed, S. Ganapathy-Kanniappan, R. Kunjithapatham, J. W. Wijlemans, B. Kook Kwak, S. Ota, M. Vali, Spontaneous tumor regression in a syngeneic rat model of liver cancer: Implications for survival studies. *J. Vasc. Interv. Radiol.* **23**, 1685–1691 (2012).

70. J. B. Mathieu, S. Martel, Steering of aggregating magnetic microparticles using propulsion gradients coils in an MRI scanner. *Magn. Reson. Med.* **63**, 1336–1345 (2010).

71. G. Go, J. Han, J. Zhen, S. Zheng, A. Yoo, M.-J. Jeon, J.-O. Park, S. Park, A magnetically actuated microscaffold containing mesenchymal stem cells for articular cartilage repair. *Adv. Healthc. Mater.* **6**, 1601378 (2017).

72. A. J. Petruska, B. J. Nelson, Minimum bounds on the number of electromagnets required for remote magnetic manipulation. *IEEE Trans. Robot.* **31**, 714–722 (2015).

73. A. Pourkand, J. J. Abbott, A critical analysis of eight-electromagnet manipulation systems: The role of electromagnet configuration on strength, isotropy, and access. *IEEE Robot. Autom. Lett.* **3**, 2957–2962 (2018).

74. M. P. Kummer, J. J. Abbott, B. E. Kratochvil, R. Borer, A. Sengul, B. J. Nelson, OctoMag: An electromagnetic system for 5-DOF wireless micromanipulation. *IEEE Trans. Robot.* **26**, 1006–1017 (2010).

75. W. L. Chandler, G. Schmer, Evaluation of a new dynamic viscometer for measuring the viscosity of whole blood and plasma. *Clin. Chem.* **32**, 505–507 (1986).

76. J. D. Cutnell, K. W. Johnson, Fluids, In *Physics* (Wiley, 2009), Chapter 11.